

# On the Road to Discovery of Relic Gravitational Waves: $TE$ and $BB$ Correlations in the Cosmic Microwave Background Radiation

W. Zhao,<sup>1,2,3,\*</sup> D. Baskaran,<sup>1,2,†</sup> and L. P. Grishchuk<sup>1,4,‡</sup>

<sup>1</sup>*School of Physics and Astronomy, Cardiff University, Cardiff, CF24 3AA, United Kingdom*

<sup>2</sup>*Wales Institute of Mathematical and Computational Sciences, United Kingdom*

<sup>3</sup>*Department of Physics, Zhejiang University of Technology, Hangzhou, 310014, P. R. China*

<sup>4</sup>*Sternberg Astronomical Institute, Moscow State University, Moscow 119899, Russia*

## Abstract

The detection of primordial gravitational waves is one of the biggest challenges of the present time. The existing (WMAP) observations are helpful on the road to this goal, and the forthcoming experiments (Planck) are likely to complete this mission. We show that the 5-year WMAP  $TE$  data contains a hint of the presence of gravitational wave contribution. In terms of the parameter  $R$ , which gives the ratio of contributions from gravitational waves and density perturbations to the temperature quadrupole, the best-fit model produced  $R = 0.24$ . Because of large residual noises, the uncertainty of this determination is still large, and it easily includes the  $R = 0$  hypothesis. However, the uncertainty will be strongly reduced in the forthcoming more sensitive observations. We numerically simulated the Planck data and concluded that the relic gravitational waves with  $R = 0.24$  will be present at a better than  $3\sigma$  level in the  $TE$  observational channel, and at a better than  $2\sigma$  level in the ‘realistic’  $BB$  channel. The balloon-borne and ground-based observations may provide a healthy competition to Planck in some parts of the lower- $\ell$  spectrum.

PACS numbers: 98.70.Vc, 98.80.Cq, 04.30.-w

arXiv:0810.0756v3 [astro-ph] 6 Jan 2009

---

\*Electronic address: Wen.Zhao@astro.cf.ac.uk

†Electronic address: Deepak.Baskaran@astro.cf.ac.uk

‡Electronic address: Leonid.Grishchuk@astro.cf.ac.uk

## I. INTRODUCTION

The relic gravitational waves must have been generated by strong variable gravitational field of the very early Universe [1]. We got used to the notion that the generation of gravitational waves requires some sort of a time-dependent quadrupole moment in the energy distribution of matter and fields. But, by definition, there is no such asymmetries in the distribution of matter and fields comprising a homogeneous isotropic universe. So, how the relic gravitational waves could come into existence? In the context of classical gravitational waves, the word ‘amplification’ is probably a more accurate explanation than the word ‘generation’. Indeed, the pre-existing classical gravitational waves could be amplified in the course of time, because the nonlinear character of gravitation makes them parametrically coupled to the variable gravitational field of the isotropic homogeneous universe (gravitational pump field). The coupling is strong and effective if and when the variations of the pump field are so fast that the inverse time-scale of variations becomes comparable with the frequency of the wave. This is when the amplitude of the wave increases over and above the limits of the adiabatic law.

Moreover, the phenomenon of relic gravitational waves is more general than this classical picture; it does not require the previously generated waves and does not rely on their presence. The reason is that in the quantum world there always exist, even in the absence of classical waves, the inevitable ground (vacuum) state fluctuations of the corresponding field. One can think of these zero-point quantum oscillations as those that are being amplified, as a result of their interaction with the gravitational pump field. Speaking more accurately, the quantum-mechanical Schrodinger evolution transforms the initial no-particle (vacuum) state of gravitational waves into a multi-particle (strongly squeezed vacuum) state. In this sense, relic gravitational waves have been generated from ‘nothing’ by the external pump field. This process is called the superadiabatic (parametric) amplification. For a recent review of the subject, see [2].

Under certain extra conditions, the cosmological density perturbations ( $dp$ ), which combine specific perturbations of the gravitational field and matter fields, can also be generated by the same mechanism of superadiabatic (parametric) amplification. This takes place in addition to the generation of gravitational waves ( $gw$ ). The theoretical ingredients describing the independently quantized ‘tensor’ ( $t$ , gravitational waves) and ‘scalar’ ( $s$ , density perturbations) degrees of freedom of the perturbed early Universe are almost identical. This results in approximately equal amplitudes of the long-wavelength metric perturbations representing gravitational waves on one side and density perturbations on the other side. Therefore, assuming that the observed anisotropies in cosmic microwave background radiation (CMB) are indeed caused by cosmological perturbations of quantum-mechanical origin, one expects that the contributions of density perturbations and gravitational waves to the lower-order CMB multipoles are of the same order of magnitude (see [2] and references there).

The content of the paper is as follows. In Sec. II we explain the properties of the gravitational field perturbations  $h_{ij}(\eta, \mathbf{x})$ , and summarize the definitions and notations that will be used in the paper. We shall be working with the expansion of the field  $h_{ij}$  over spatial Fourier harmonics  $e^{\pm i\mathbf{n}\cdot\mathbf{x}}$ , and with the associated Fourier coefficients  $c_{\mathbf{n}}^s$  and  $c_{\mathbf{n}}^{s\dagger}$ . In the rigorous quantum-mechanical version of the theory,  $c_{\mathbf{n}}^s$  and  $c_{\mathbf{n}}^{s\dagger}$  are the annihilation and creation operators acting on the quantum states. But, to simplify calculations, we are using a ‘classical’ version of the theory, whereby  $c_{\mathbf{n}}^s$  and  $c_{\mathbf{n}}^{s\dagger}$  are treated as classical random complex numbers  $c_{\mathbf{n}}^s$  and  $c_{\mathbf{n}}^{s*}$ .

In Sec. III we explain in detail how the statistical properties of the underlying cosmological perturbations, encoded in the probability density functions (pdf’s) of complex random variables  $c_{\mathbf{n}}^s, c_{\mathbf{n}}^{s*}$ , translate into the statistical properties of the CMB multipole coefficients  $a_{\ell m}^X$  ( $X = T, E, B$ ). The statistics of the CMB anisotropies, often referred to in the form of a loose and poetic concept of ‘cosmic variance’, is an important ingredient of the whole problem of deriving cosmological conclusions from the CMB data. We formulate the pdf’s for individual quantities  $a_{\ell m}^X$  and for the full set  $\{a_{\ell m}^X\}$  of these quantities. The main emphasis is on the correlation coefficient  $\rho_\ell$  in the joint pdf for  $T$  and  $E$  components of the CMB.

In Sec. IV we formulate the pdf’s for the best unbiased estimators of the auto-correlation and cross-correlation power spectra. Again, the main emphasis is on the estimator  $D_\ell^{TE}$  of the  $TE$  power spectrum. This is because the gravitational waves have a distinctive signature in the region of lower  $\ell$ ’s: the mean value of  $D_\ell^{TE}$  must be positive for density perturbations and negative for gravitational waves [3]. The individual outcomes may have signs opposite to the sign of the mean value. This is why we evaluate the probabilities of finding positive (negative) outcomes for  $D_\ell^{TE}$  in the situation when the expected value of this variable is negative (positive).

The actual numerical amount of the  $TE$  cross-correlation at every  $\ell$  is governed by the numerical value of the correlation coefficient  $\rho_\ell$ . In Sec. V we derive  $\rho_\ell$  for specific cosmological models with various amounts of density perturbations and gravitational waves. The parameters of the background cosmological model are always taken from the 5-year Wilkinson Microwave Anisotropy Probe (WMAP) best-fit  $\Lambda$ CDM cosmology [4], but the perturbation parameters are allowed to vary. The derived coefficients  $\rho_\ell$  make it possible to build the  $\ell$ -dependent confidence intervals surrounding the mean value of the estimator  $D_\ell^{TE}$ .

The inherent uncertainty of the expected CMB signal, ultimately explicable in terms of the quantum-mechanical origin of cosmological perturbations, is exacerbated by the ‘real life’ effects, such as instrumental noises, foreground emissions, incomplete sky coverage, etc. In Sec. VI we use the parameters of the WMAP and Planck missions to show how these effects broaden the size of the confidence intervals. This allows us to put to the test the existing WMAP  $TE$  data and make predictions for the Planck mission.

The WMAP5 best-fit analysis suggests that the observed CMB anisotropies have no contribution from gravitational waves [4]. We call this conclusion the null hypothesis  $H_0$ . In Sec. VII we test the null hypothesis using the WMAP5  $TE$  data. Although the evidence for rejection of  $H_0$  is weak, within  $1\sigma$ , the data points demonstrate the tendency to lie below the  $H_0$  expectation curve, which is actually required by the presence of relic gravitational waves.

Since the existence of relic gravitational waves is a necessity dictated by general relativity and quantum mechanics, we include gravitational waves in the  $TE$  data analysis as a compulsory ingredient (Sec. VIII). We consider a class of models which contain gravitational waves and are consistent with the available  $TT$ ,  $EE$  and  $BB$  data. Although our physical picture is guided by gravitational waves of quantum-mechanical origin [2], the analysis is general and applies to gravitational waves of any origin. One has to note, though, that classical gravitational waves generated at later stages of cosmological evolution have wavelengths much shorter than the Hubble radius and therefore they do not affect the lower-order CMB multipoles. We build and study the likelihood function for  $R$ , where  $R$  is the ratio of  $gw$  and  $dp$  contributions to the temperature quadrupole  $C_{\ell=2}^{TT}$ . The maximum of the likelihood function turns out to be at  $R = 0.24$ . This number also determines other perturbation parameters in our class of models. Because of the large WMAP noises, the confidence interval for  $R$  is quite broad, so that the WMAP team’s suggestion  $R = 0$  is only  $1\sigma$  away from our maximum likelihood value  $R = 0.24$ . Nevertheless, we consider our best-fit model with  $R = 0.24$  as a benchmark model, which we believe is to be confirmed by the more sensitive Planck mission. We numerically simulate the future Planck data and show that the relic gravitational waves are to be detected by the  $TE$  method at a better than  $3\sigma$  level.

The prospects of the Planck mission are discussed at some length in the last Sec. IX. We compare the  $TE$  method with the more often mentioned  $BB$  method. The  $B$ -mode of polarization does not contain the contribution from density perturbations but is inherently weak and prone to various systematic effects. We distinguish the ‘optimistic’ and ‘realistic’ cases in detection of gravitational waves through the  $BB$  correlation function. It appears that the ‘realistic’  $BB$  case offers a little better than  $2\sigma$  detection of relic gravitational waves in the  $R = 0.24$  model. We also show that the  $BB$  method mostly relies on the reionization era, whereas the  $TE$  correlation function is mostly sensitive to the era of recombination.

The Conclusions summarize our findings and emphasize the necessity of concentrated efforts in the race for discovery of relic gravitational waves.

## II. GRAVITATIONAL FIELD PERTURBATIONS

Let us recall that the gravitational field of a slightly perturbed flat Friedmann-Lemaitre-Robertson-Walker (FLRW) universe is described by

$$ds^2 = -c^2 dt^2 + a^2(t)(\delta_{ij} + h_{ij})dx^i dx^j = a^2(\eta)[-d\eta^2 + (\delta_{ij} + h_{ij})dx^i dx^j],$$

where  $t$ -time and  $\eta$ -time are related by  $cdt = a d\eta$ . The metric perturbation field  $h_{ij}(\eta, \mathbf{x})$  can be expanded over spatial Fourier harmonics  $e^{\pm i\mathbf{n}\cdot\mathbf{x}}$ :

$$h_{ij}(\eta, \mathbf{x}) = \frac{\mathcal{C}}{(2\pi)^{3/2}} \int_{-\infty}^{+\infty} \frac{d^3\mathbf{n}}{\sqrt{2n}} \sum_{s=1,2} \left[ \overset{s}{p}_{ij}(\mathbf{n}) \overset{s}{h}_n(\eta) e^{i\mathbf{n}\cdot\mathbf{x}} \overset{s}{c}_{\mathbf{n}} + \overset{s}{p}_{ij}^*(\mathbf{n}) \overset{s}{h}_n^*(\eta) e^{-i\mathbf{n}\cdot\mathbf{x}} \overset{s}{c}_{\mathbf{n}}^\dagger \right], \quad (1)$$

where  $\mathbf{n}$  is the dimensionless time-independent wavevector. The dimensionless wavenumber  $n$  is  $n = (\delta_{ij} n^i n^j)^{1/2}$ .

The dimensionless  $n$  is related with the dimensionful  $k$  by  $k = n/2l_H$ , where  $l_H = c/H_0$  is today’s Hubble radius. The value  $n_H = 4\pi$  labels the wave whose today’s wavelength is equal to the ‘half of the size of the Universe’, that is, equal to today’s Hubble radius. The use of  $n$ , rather than  $k$ , is very convenient as it guides the evaluation of the CMB multipoles: cosmological perturbations with wavenumber  $n$  are mostly responsible for the CMB temperature anisotropies at the multipole  $\ell \approx n$ .

The general form of Eq. (1) is common for metric perturbations  $h_{ij}(\eta, \mathbf{x})$  characterizing gravitational waves and density perturbations, but they differ in the explicit content of the two polarization tensors  $\overset{s}{p}_{ij}(\mathbf{n})$  ( $s = 1, 2$ ). In the  $gw$  case the field  $h_{ij}$  consists of two ‘transverse-traceless’ components, whereas in the  $dp$  case it consists of the ‘scalar’ and ‘longitudinal-longitudinal’ components (see, for example, [3]). The  $gw$  mode functions  $\overset{s}{h}_n(\eta)$  satisfy the perturbed Einstein equations linearized around an FLRW background. In the  $dp$  case the gravitational mode functions

$\overset{s}{h}_n(\eta)$  are necessarily accompanied by matter mode functions. For many models of matter, the full set of dynamical equations for density perturbations leaves independent only one out of two polarization components  $s = 1, 2$ .

In the rigorous quantum-mechanical version of the theory, the quantities  $h_{ij}$  are quantum-mechanical operators acting on quantum states. The  $\overset{s}{c}_{\mathbf{n}}$  and  $\overset{s}{c}_{\mathbf{n}}^\dagger$  are the annihilation and creation operators, satisfying the commutation relationships  $[\overset{s'}{c}_{\mathbf{n}}, \overset{s}{c}_{\mathbf{n}'}^\dagger] = \delta_{s's'}\delta^{(3)}(\mathbf{n} - \mathbf{n}')$ . In the case of density perturbations, the same operators  $\overset{s}{c}_{\mathbf{n}}$  and  $\overset{s}{c}_{\mathbf{n}}^\dagger$  are inherited, through the linearized Einstein equations, by the matter fields. According to the physical formulation of the problem, the initial quantum state of the quantized perturbations is the ground state  $|0\rangle$  of the corresponding Hamiltonian. The ground state satisfies the condition  $\overset{s}{c}_{\mathbf{n}}|0\rangle = 0$ . For gravitational waves, the normalization constant  $\mathcal{C}$  is  $\mathcal{C} = \sqrt{16\pi}l_{\text{Pl}}$ , whereas for density perturbations  $\mathcal{C} = \sqrt{24\pi}l_{\text{Pl}}$ , where  $l_{\text{Pl}} = (G\hbar/c^3)^{1/2}$  is the Planck length. Obviously, if the Planck constant  $\hbar$  is artificially sent to zero, the initial zero-point quantum fluctuations, as well as the field  $h_{ij}$  itself, vanish.

To simplify calculations, we will be using a ‘classical’ version of the theory, whereby the quantum-mechanical operators  $\overset{s}{c}_{\mathbf{n}}$  and  $\overset{s}{c}_{\mathbf{n}}^\dagger$  are treated as classical random complex numbers  $\overset{s}{c}_{\mathbf{n}}$  and  $\overset{s}{c}_{\mathbf{n}}^*$ . We are losing some delicate quantum aspects of the rigorous theory but they are not the matter of our major concern. The statistical properties of  $\overset{s}{c}_{\mathbf{n}}$ ,  $\overset{s}{c}_{\mathbf{n}}^*$  define the statistical properties of the classical field  $h_{ij}$  (1) and, through the linear radiative transfer equations, they determine the statistical properties of the CMB anisotropies.

Since the Schrodinger evolution of the initial vacuum state into a squeezed vacuum state retains the Gaussianity of the state (while developing strongly unequal variances in the amplitude and the phase), we are justified in assuming that each individual complex coefficient  $\overset{s}{c}_{\mathbf{n}}$  is described by a complex pdf [5, 6] with a zero mean and unit variance. If necessary, one can imagine that the space of wavevectors  $\mathbf{n}$  is discretised into a fine 3-lattice. Moreover, since the different modes  $\mathbf{n}$  and polarization states  $s$  are not supposed to ‘know about each other’, we are justified in assuming that the joint distribution for all coefficients  $\{\overset{s}{c}_{\mathbf{n}}\}$  (that is, for the full set including all possible values of  $\mathbf{n}$  and  $s$ ) is a complex multivariate Gaussian pdf comprising a product of individual Gaussian pdf’s [5, 6].

The first and the second moments calculated with the joint pdf amount to

$$\langle \overset{s}{c}_{\mathbf{n}} \rangle = \langle \overset{s}{c}_{\mathbf{n}}^* \rangle = 0, \quad \langle \overset{s}{c}_{\mathbf{n}} \overset{s'}{c}_{\mathbf{n}'}^* \rangle = \delta_{ss'}\delta^{(3)}(\mathbf{n} - \mathbf{n}'), \quad \langle \overset{s}{c}_{\mathbf{n}} \overset{s'}{c}_{\mathbf{n}'} \rangle = \langle \overset{s}{c}_{\mathbf{n}}^* \overset{s'}{c}_{\mathbf{n}'}^* \rangle = 0. \quad (2)$$

Since the coefficients  $\overset{s}{c}_{\mathbf{n}}$  obey a joint multivariate Gaussian (normal) distribution, the higher order averages are expressible in terms of the second moments.

It is clear from Eq. (2) that the mean value of the field  $h_{ij}$  is zero, but the variance is non-zero and is calculated to be

$$\frac{1}{2}\langle h_{ij}(\eta, \mathbf{x})h^{ij}(\eta, \mathbf{x}) \rangle = \int_0^\infty \frac{dn}{n} h^2(n, \eta).$$

The function

$$h^2(n, \eta) \equiv \frac{\mathcal{C}^2}{2\pi^2}n^2 \sum_{s=1,2} |\overset{s}{h}_n(\eta)|^2, \quad (3)$$

gives the mean-square value of the gravitational field perturbations in a logarithmic interval of the wavenumbers  $n$ . It is called the metric power spectrum. The spectrum (3) refers to gravitational waves or density perturbations depending on whether this quantity is calculated from  $gw$  or  $dp$  mode functions.

The CMB calculations are usually being done numerically, whereby the initial conditions for differential equations are imposed at times deep in the radiation-dominated era [7, 8]. The wavelengths of relevant modes  $\mathbf{n}$  are much longer than the Hubble radius at that time, and the primordial power spectrum  $h^2(n)$  is a smooth function of  $n$ . The early pump fields (scale factors)  $a(\eta)$  which are power-law functions of  $\eta$  generate primordial spectra  $h^2(n)$  which are power-law functions of  $n$  [2]:

$$h^2(n)(gw) = B_t^2 n^{n_t}, \quad h^2(n)(dp) = B_s^2 n^{n_s-1}. \quad (4)$$

The quantum-mechanical evolution of the initial vacuum states of  $gw$  and  $dp$  fields results [2] in approximately equal primordial amplitudes  $B_t^2$ ,  $B_s^2$ , and also in the relationship  $n_t \approx n_s - 1$ . Although, in general, the four numbers  $B_t^2$ ,  $B_s^2$ ,  $n_t$ ,  $n_s$  specified at the radiation-dominated stage do not contain enough information to impose all the starting conditions for numerical calculation of the ensuing CMB anisotropies, some additional simplifying assumptions [7, 8], [3] allow one to do that.

At the end of this section it is necessary to warn the reader that according to the claims of inflationary theory the amplitudes of density perturbations should be arbitrarily large in the limit of models with small values of the early Universe parameter  $\epsilon$ , where  $\epsilon = -\dot{H}/H^2$ . Specifically, the incorrect (inflationary) treatment of quantized scalar perturbations has led to the proposition that the power spectrum of scalar metric perturbations (often denoted by  $\zeta$  or  $\mathcal{R}$ ) should be divergent as  $1/\epsilon$ , right from the very early times of imposing initial conditions in the high-frequency regime of the perturbations. This predicted divergency of density perturbations in the limit of  $\epsilon = 0$  ( $n_s = 1, n_t = 0$ ) is customarily being substituted by the claim that it is the amount of primordial gravitational waves that is expected to be very small. This is expressed in the form of small values of the ‘tensor-to-scalar’ ratio  $r$ :

$$r = 16\epsilon = -8n_t. \quad (5)$$

In particular, according to the inflationary Eq. (5), the interval of a ‘standard’ (de Sitter) inflation, i.e.  $\epsilon = 0$ , generates a zero amount of primordial gravitational waves, i.e.  $r = 0$ . This is in full contradiction with the mechanism of superadiabatic (parametric) amplification [1]. Certainly, we are not using Eq. (5), neither as a valid theoretical result nor as an element of CMB data analysis. For a detailed critical discussion of inflationary predictions and the data analysis based on inflationary theory, see [2].

### III. ANISOTROPIES IN THE COSMIC MICROWAVE BACKGROUND RADIATION

#### A. Characterization of the radiation field

The radiation field is usually characterized by four Stokes parameters ( $I, Q, U, V$ ), where  $I$  is the total intensity of radiation,  $Q$  and  $U$  describe the magnitude and direction of linear polarization, and  $V$  is the circular polarization. The Stokes parameters can be viewed as functions of  $(t, x^i, \nu, e^i)$ , where  $\nu$  is the photon’s frequency, and  $e^i$  is a unit vector in the direction of observation (opposite to the photon’s propagation). In a given space-time point  $(t, x^i)$  and for a fixed  $\nu$ , the Stokes parameters are functions of  $\theta, \phi$ , where  $\theta, \phi$  are coordinates on a unit sphere indicating the direction of observation:  $d\sigma^2 = g_{ab}dx^a dx^b = d\theta^2 + \sin^2\theta d\phi^2$ .

The Stokes parameters of the radiation are components of the polarization tensor  $P_{ab}$  [9] which can be written as

$$P_{ab}(\theta, \phi) = \frac{1}{2} \begin{pmatrix} I + Q & -(U - iV) \sin \theta \\ -(U + iV) \sin \theta & (I - Q) \sin^2 \theta \end{pmatrix}.$$

Under arbitrary transformation of coordinates  $(\theta, \phi)$ , the components of  $P_{ab}(\theta, \phi)$  transform as components of a tensor, but some combinations of  $P_{ab}(\theta, \phi)$  and its derivatives remain invariant.

Two algebraic invariants are given by

$$I(\theta, \phi) = g^{ab}(\theta, \phi)P_{ab}(\theta, \phi), \quad V(\theta, \phi) = i\epsilon^{ab}(\theta, \phi)P_{ab}(\theta, \phi),$$

where  $\epsilon^{ab}(\theta, \phi)$  is a completely antisymmetric pseudotensor

$$\epsilon^{ab} = \begin{pmatrix} 0 & -\sin^{-1}\theta \\ \sin^{-1}\theta & 0 \end{pmatrix}.$$

Now one can single out the symmetric trace-free (STF) part  $P_{ab}^{\text{STF}}$  of  $P_{ab}$ :  $P_{ab}(\theta, \phi) = \frac{1}{2}I g_{ab} - \frac{i}{2}V \epsilon_{ab} + P_{ab}^{\text{STF}}$ ,

$$P_{ab}^{\text{STF}} = \frac{1}{2} \begin{pmatrix} Q & -U \sin \theta \\ -U \sin \theta & -Q \sin^2 \theta \end{pmatrix}.$$

Two other invariants require the use of second covariant derivatives of  $P_{ab}^{\text{STF}}$ . It can be shown that there exist only two linearly independent invariants that can be built from second derivatives [3]:

$$E(\theta, \phi) = -2(P_{ab}^{\text{STF}})^{;a;b}, \quad B(\theta, \phi) = -2(P_{ab}^{\text{STF}})^{;b;d} \epsilon_d^a.$$

In the above expression “;” denotes covariant differentiation on the sphere. The quantities  $I$  and  $E$  are scalars, while  $V$  and  $B$  are pseudoscalars.

In CMB applications one usually ignores  $V$ , as well as the unperturbed part of  $I$ , and regards the remaining quantities as measured in the temperature units, specifically in micro-Kelvin ( $\mu\text{K}$ ). These quantities (temperature and polarization anisotropies) can be expanded over ordinary spherical harmonics  $Y_{\ell m}(\theta, \phi)$ :

$$I(\theta, \phi) = \sum_{\ell=0}^{\infty} \sum_{m=-\ell}^{\ell} a_{\ell m}^T Y_{\ell m}(\theta, \phi), \quad (6a)$$

$$E(\theta, \phi) = \sum_{\ell=2}^{\infty} \sum_{m=-\ell}^{\ell} \left[ \frac{(\ell+2)!}{(\ell-2)!} \right]^{\frac{1}{2}} a_{\ell m}^E Y_{\ell m}(\theta, \phi), \quad B(\theta, \phi) = \sum_{\ell=2}^{\infty} \sum_{m=-\ell}^{\ell} \left[ \frac{(\ell+2)!}{(\ell-2)!} \right]^{\frac{1}{2}} a_{\ell m}^B Y_{\ell m}(\theta, \phi). \quad (6b)$$

The  $\ell$ -dependent factors in front of  $a_{\ell m}^E$  and  $a_{\ell m}^B$  in (6b) have been introduced in order to work with definitions consistent with previous literatures [8], [10].

Since  $I, E, B$  are real functions on the sphere, the complex multipole coefficients in (6a) and (6b) satisfy the following conditions

$$a_{\ell m}^X = (-1)^m a_{\ell, -m}^{X*}, \quad (X = T, E, B, \quad -\ell \leq m \leq \ell). \quad (7)$$

The set of multipole coefficients  $(a_{\ell m}^T, a_{\ell m}^E, a_{\ell m}^B)$  completely characterizes the CMB field that we are studying.

## B. Statistical properties of the CMB field

The radiative transfer equations relate the set of random coefficients  $\overset{s}{c}_{\mathbf{n}}$  with the multipole coefficients  $(a_{\ell m}^T, a_{\ell m}^E, a_{\ell m}^B)$ . As a consequence, the multipole coefficients  $a_{\ell m}^X$  ( $X = T, E, B$ ) inherit the randomness of  $\overset{s}{c}_{\mathbf{n}}$ .

The calculations usually begin from a single Fourier mode of perturbations considered in a special reference frame whose  $z$ -axis is parallel to the wavevector  $\mathbf{n}$ . This is how one arrives at the multipole coefficients denoted  $a_{\ell m}^X(n, s)$ . The quantities  $a_{\ell m}^X(n, s)$  depend in a complicated but calculable manner on the metric (plus matter, in the case of density perturbations) mode functions and the background cosmological model [11, 12, 13, 14, 15, 16, 17, 18, 19, 20, 21, 22], [3], [23]. The next step is the generalization of this result to the set of all Fourier components with arbitrarily directed  $\mathbf{n}$ 's. This requires the use of the Wigner rotation coefficients  $D_{mm'}^{\ell}(\hat{\mathbf{n}})$ , where  $\hat{\mathbf{n}} \equiv \mathbf{n}/n$ . The Wigner coefficients describe the rotation of individual special frames associated with  $\mathbf{n}$ 's to one unique frame of the observer. The Wigner coefficients satisfy the orthogonality relation [24]

$$(2\ell+1) \int D_{mm'}^{\ell}(\hat{\mathbf{n}}) D_{MM'}^{\ell}(\hat{\mathbf{n}}) d\Omega_{\hat{\mathbf{n}}} = 4\pi \delta_{\ell L} \delta_{mM} \delta_{m'M'}. \quad (8)$$

A detailed analysis shows [3] that the resulting multipole coefficients  $a_{\ell m}^X$  are related to the random coefficients  $\overset{s}{c}_{\mathbf{n}}$ , both for  $gw$  and  $dp$ , as follows

$$a_{\ell m}^X = \frac{\mathcal{C}}{(2\pi)^{3/2}} \int_{-\infty}^{\infty} \frac{d^3\mathbf{n}}{\sqrt{2n}} \sum_{s=1,2} \sum_{m'=-\ell}^{\ell} \left[ a_{\ell m'}^X(n, s) D_{mm'}^{\ell}(\hat{\mathbf{n}}) \overset{s}{c}_{\mathbf{n}} + (-1)^m a_{\ell m'}^{X*}(n, s) D_{-m, m'}^{\ell}(\hat{\mathbf{n}}) \overset{s}{c}_{\mathbf{n}}^* \right]. \quad (9)$$

The linear character of this relation implies that the probability density functions of individual multipole coefficients  $a_{\ell m}^X$  are zero-mean Gaussian pdf's, and the joint distribution of all multipole coefficients is described by a multivariate Gaussian pdf. The effects of nonlinearities and quantum loops of the underlying metric field are very small, and we ignore them. The nonlinear effects in the radiative transfer equations are possible, but apparently they are also small. The individual distributions are marginal distributions derivable from the joint pdf. Before formulating these pdf's explicitly, we shall use Eq. (2) and Eq. (9) in order to find second moments of the distributions.

### 1. Auto-correlation and cross-correlation functions

It follows from Eq. (2) and Eq. (9) that all linear averages of  $a_{\ell m}^X$  vanish,

$$\langle a_{\ell m}^X \rangle = \langle a_{\ell m}^{X*} \rangle = 0.$$

The quadratic averages  $\langle a_{\ell m}^X a_{\ell' m'}^{X'*} \rangle$  do not vanish. They are called the correlation functions. One gets an auto-correlation function if  $X = X'$ , and a cross-correlation function if  $X \neq X'$ .

Let us start from the auto-correlation functions [15, 17, 18, 22], [3], [23]. Using Eqs. (2, 9, 8) one can show that

$$\langle a_{\ell m}^X a_{\ell' m'}^{X'*} \rangle = \delta_{m m'} \delta_{\ell \ell'} C_{\ell}^{XX}, \quad \langle a_{\ell m}^X a_{\ell' m'}^X \rangle = \langle a_{\ell m}^{X*} a_{\ell' m'}^{X*} \rangle = 0, \quad (X = T, E, B), \quad (10)$$

where the  $XX$  power spectrum  $C_\ell^{XX}$  is given by [3]

$$C_\ell^{XX} = \frac{\mathcal{C}^2}{2\pi^2(2\ell+1)} \int ndn \sum_{s=1,2} \sum_{m=-\ell}^{\ell} |a_{\ell m}^X(n, s)|^2. \quad (11)$$

Both, density perturbations and gravitational waves, produce distinctive  $C_\ell^{TT}$ ,  $C_\ell^{EE}$  power spectra, but the  $C_\ell^{BB}$  is zero for density perturbations and  $C_\ell^{BB} \neq 0$  for gravitational waves [8, 10, 25, 26]. Specifically, all the coefficients  $a_{\ell m}^B(n, s)$  vanish in the  $dp$  case. In other words, density perturbations do not produce the  $B$ -mode of polarization [8, 10, 25, 26], [3].

Let us now turn to the cross-correlation functions. In general, there exists three cross-correlation functions, namely  $TE$ ,  $TB$  and  $EB$ . However, the  $TB$  and  $EB$  functions vanish identically in the  $dp$  case, as density perturbations do not produce the  $B$ -mode. In the  $gw$  case, the left and right circular polarizations of gravitational waves give contributions of opposite signs into the  $TB$  and  $EB$  functions. It is very natural to expect that the relic gravitational waves with both polarizations had been generated in equal amounts. Then, one concludes that in the  $gw$  case the  $TB$  and  $EB$  functions do also vanish [27], [3]. (However, there exist parity-violating processes in the later Universe, see for example [28].) Therefore, we shall only deal with the  $TE$  cross-correlation function.

Using Eqs. (9, 2, 8), we arrive at

$$\begin{aligned} \frac{1}{2} \langle a_{\ell m}^T a_{\ell' m'}^{E*} + a_{\ell m}^{T*} a_{\ell' m'}^E \rangle &= \delta_{mm'} \delta_{\ell\ell'} C_\ell^{TE}, \quad \frac{1}{2} \langle a_{\ell m}^T a_{\ell' m'}^{E*} - a_{\ell m}^{T*} a_{\ell' m'}^E \rangle = 0, \\ \langle a_{\ell m}^T a_{\ell' m'}^E \rangle &= \langle a_{\ell m}^{T*} a_{\ell' m'}^{E*} \rangle = 0, \end{aligned} \quad (12)$$

where the  $C_\ell^{TE}$  is given by

$$C_\ell^{TE} = \frac{\mathcal{C}^2}{4\pi^2(2\ell+1)} \int ndn \sum_{s=1,2} \sum_{m=-\ell}^{\ell} [a_{\ell m}^T(n, s) a_{\ell m}^{E*}(n, s) + a_{\ell m}^{T*}(n, s) a_{\ell m}^E(n, s)]. \quad (13)$$

Note that one can derive Eqs. (10, 12) as soon as the averages (2) are given, independently on whether the actual distributions are Gaussian or not. Also, it is seen from Eqs. (10, 12) that only the products of coefficients with  $\ell = \ell'$  and  $m = m'$  are important.

Unlike the auto-correlation power spectra  $C_\ell^{XX}$  which are strictly positive functions, the values of the  $TE$  ‘power spectrum’  $C_\ell^{TE}$  can be positive or negative. Most importantly for our further discussion, in the region of lower  $\ell$ 's the function  $C_\ell^{TE}$  is positive for density perturbations and negative for gravitational waves [3]. It can also be shown, using Eqs. (13, 11), that

$$(C_\ell^{TE})^2 \leq C_\ell^{TT} C_\ell^{EE}, \quad (14)$$

which is the analog of the Cauchy-Bunyakovsky-Schwarz inequality.

Since density perturbations and gravitational waves are independent fields, they contribute to the total CMB power spectra additively:

$$C_\ell^{XX'} = C_\ell^{XX'}(dp) + C_\ell^{XX'}(gw). \quad (15)$$

## 2. Probability density functions for individual multipole coefficients

The Gaussian nature of  $\tilde{c}_n$ , together with Eq. (9), translate into Gaussian pdf's for individual multipole coefficients  $a_{\ell m}^X$ .

It is convenient to start from distributions for real and imaginary parts of  $a_{\ell m}^X$ ,

$$a_{\ell m}^X = a_{\ell m}^{X(r)} + i a_{\ell m}^{X(i)}.$$

It follows from Eq. (7) that

$$a_{\ell 0}^{X(i)} = 0, \quad a_{\ell m}^{X(r)} = (-1)^m a_{\ell, -m}^{X(r)}, \quad \text{and} \quad a_{\ell m}^{X(i)} = (-1)^{m+1} a_{\ell, -m}^{X(i)}.$$

Thus, the set of multipole coefficients  $a_{\ell m}^X$ , where  $\ell \geq m \geq -\ell$ , is fully equivalent to the set of real quantities  $a_{\ell 0}^{X(r)}$ ,  $a_{\ell m}^{X(r)}$ ,  $a_{\ell m}^{X(i)}$ , where  $\ell \geq m \geq 1$ . We will be using index  $c$  to denote all quantities as  $a_{\ell m}^{X(c)}$  where  $c = r$  or  $i$  if  $m \geq 1$ , and  $c = r$  if  $m = 0$ .

Each individual coefficient  $a_{\ell m}^{X(c)}$  satisfies a zero-mean normal distribution

$$f(a_{\ell m}^{X(c)}) = \frac{1}{\sqrt{2\pi}\sigma_{\ell m}^{X(c)}} e^{-(a_{\ell m}^{X(c)})^2/2(\sigma_{\ell m}^{X(c)})^2}.$$

The variances, i.e. the squares of standard deviations  $\sigma_{\ell m}^{X(c)}$ , are the second moments already analyzed in the previous subsection. Comparing with Eq. (10) one finds

$$\begin{aligned} (\sigma_{\ell 0}^{X(r)})^2 &= \langle a_{\ell 0}^{X(r)} a_{\ell 0}^{X(r)} \rangle = C_{\ell}^{XX}, \\ (\sigma_{\ell m}^{X(r)})^2 &= \langle a_{\ell m}^{X(r)} a_{\ell m}^{X(r)} \rangle = \frac{1}{2} C_{\ell}^{XX}, \quad (\sigma_{\ell m}^{X(i)})^2 = \langle a_{\ell m}^{X(i)} a_{\ell m}^{X(i)} \rangle = \frac{1}{2} C_{\ell}^{XX}, \quad (\ell \geq m \geq 1) \\ \langle a_{\ell m}^{X(r)} a_{\ell m}^{X(i)} \rangle &= 0. \end{aligned}$$

Denoting  $\sigma_{\ell}^X = \sqrt{C_{\ell}^{XX}}$ , one can write:  $\sigma_{\ell 0}^X = \sigma_{\ell}^X$  and  $\sigma_{\ell m}^{X(r)} = \sigma_{\ell m}^{X(i)} = \sigma_{\ell}^X/\sqrt{2}$ . In other words, the standard deviations of the  $(2\ell + 1)$  random variables  $\frac{a_{\ell 0}^{X(r)}}{\sqrt{2}}, a_{\ell m}^{X(r)}, a_{\ell m}^{X(i)}$ , where  $\ell \geq m \geq 1$ , are all equal and amount to one and the same number  $\sigma_{\ell}^X/\sqrt{2}$ .

The equivalent statements follow from the pdf for complex multipole coefficients  $a_{\ell m}^X$  ( $m \geq 1$ ). Each individual  $a_{\ell m}^X$  obeys a complex zero-mean normal distribution [5, 6] with the standard deviation  $\sigma_{\ell}^X$ :

$$f(a_{\ell m}^X) = \frac{1}{\pi(\sigma_{\ell}^X)^2} e^{-(a_{\ell m}^X a_{\ell m}^{X*})/(\sigma_{\ell}^X)^2}. \quad (16)$$

### 3. Joint probability density function for multipole coefficients

Although the joint pdf for the set of all coefficients  $\mathring{c}_{\mathbf{n}}$  is a factorizable Gaussian distribution, the radiative transfer equations make similar factorization impossible for some subsets of all multipole coefficients  $a_{\ell m}^X$ . Specifically,  $a_{\ell m}^T$  and  $a_{\ell' m'}^E$  ‘do know about each other’, when  $\ell = \ell', m = m'$ . Their joint pdf is not factorizable and their correlations do not vanish, as was made clear in Eq. (12).

Let us denote sets of coefficients by curly brackets. The full set of all multipole coefficients  $\{a_{\ell m}^X\}$  is

$$\{a_{\ell m}^X\} \equiv (a_{\ell m}^X | X = T, E, B; \ell = 2, 3, \dots; m = -\ell, \dots, \ell).$$

In this set we did not include the potentially nonzero coefficients  $a_{00}^T, a_{1m}^T$ , and hence, from now on, we restrict our analysis to multipoles  $\ell \geq 2$ .

Each member of the set  $\{a_{\ell m}^X\}$  is a linear combination (9) of complex coefficients  $\mathring{c}_{\mathbf{n}}$  whose joint distribution is a zero-mean normal pdf. This guarantees that the joint distribution for the set  $\{a_{\ell m}^X\}$  is a zero-mean multivariate normal distribution [5]. Such distributions are completely characterized by their second moments. For the physical reasons explained in Sec. III B 1 we assumed that there is no  $TB$  and  $EB$  second moments, so that the  $B$  components ‘do not know’ about  $T$  and  $E$  components. As for the non-vanishing second moments, they were calculated in Eq. (10) and Eq. (12).

Combining the above statements into a formula, we can write the joint pdf for the full set  $\{a_{\ell m}^X\}$ :

$$f(\{a_{\ell m}^T, a_{\ell m}^E, a_{\ell m}^B\}) = f(\{a_{\ell m}^T, a_{\ell m}^E\})f(\{a_{\ell m}^B\}).$$

Here,

$$f(\{a_{\ell m}^B\}) = \prod_{\ell=2}^{\infty} \prod_{m=-\ell}^{\ell} f(a_{\ell m}^B),$$

where each of the functions  $f(a_{\ell m}^B)$  (for fixed  $\ell$  and  $m$ ) is a single-variable normal distribution (16) with  $X = B$ . As for the  $T, E$  part of the joint pdf, we are interested in the subset of all  $a_{\ell m}^T, a_{\ell' m'}^E$ , in which  $\ell = \ell', m = m'$ . This part of the joint pdf is the product of the functions  $f(a_{\ell m}^T, a_{\ell m}^E)$ , for each fixed pair of  $\ell$  and  $m$ , which we are set to formulate.

The joint distribution for complex  $a_{\ell m}^T, a_{\ell m}^E$  ( $m \neq 0$ ) is a bivariate normal distribution which can be written as [5]

$$f(a_{\ell m}^T, a_{\ell m}^E) = \frac{1}{\pi^2(\sigma_{\ell}^T \sigma_{\ell}^E)^2(1 - \rho_{\ell}^2)} \exp \left\{ -\frac{1}{1 - \rho_{\ell}^2} \left[ \frac{a_{\ell m}^T a_{\ell m}^{T*}}{(\sigma_{\ell}^T)^2} + \frac{a_{\ell m}^E a_{\ell m}^{E*}}{(\sigma_{\ell}^E)^2} - \frac{\rho_{\ell}(a_{\ell m}^T a_{\ell m}^{E*} + a_{\ell m}^{T*} a_{\ell m}^E)}{\sigma_{\ell}^T \sigma_{\ell}^E} \right] \right\}. \quad (17)$$



In the case  $m = 0$ , the joint pdf reduces to a bivariate normal distribution for real quantities  $a_{\ell 0}^T, a_{\ell 0}^E$ ,

$$f(a_{\ell 0}^T, a_{\ell 0}^E) = \frac{1}{2\pi\sigma_\ell^T\sigma_\ell^E\sqrt{1-\rho_\ell^2}} \exp\left\{-\frac{1}{2(1-\rho_\ell^2)}\left[\frac{(a_{\ell 0}^T)^2}{(\sigma_\ell^T)^2} + \frac{(a_{\ell 0}^E)^2}{(\sigma_\ell^E)^2} - \frac{2\rho_\ell a_{\ell 0}^T a_{\ell 0}^E}{\sigma_\ell^T\sigma_\ell^E}\right]\right\}. \quad (18)$$

The  $\sigma_\ell^T$  and  $\sigma_\ell^E$  in Eq. (17) and Eq. (18) are the standard deviations of  $a_{\ell m}^T$  and  $a_{\ell m}^E$ , respectively. The  $\rho_\ell$  in Eq. (17) is the correlation coefficient, defined by

$$\rho_\ell = \frac{\frac{1}{2}\langle a_{\ell m}^T a_{\ell m}^{E*} + a_{\ell m}^{T*} a_{\ell m}^E \rangle}{\sqrt{\langle a_{\ell m}^T a_{\ell m}^{T*} \rangle \langle a_{\ell m}^E a_{\ell m}^{E*} \rangle}} = \frac{C_\ell^{TE}}{\sqrt{C_\ell^{TT} C_\ell^{EE}}}. \quad (19)$$

Like the standard deviation  $\sigma_\ell^X$ , which, for a given  $\ell$ , is one and the same for all  $m$ 's, the correlation coefficient  $\rho_\ell$  is also one and the same for all  $m$ 's,  $\ell \geq m \geq -\ell$ . For a bivariate normal distribution the correlation coefficient obeys the condition  $|\rho_\ell| \leq 1$ , which essentially is Eq. (14). Concrete numerical values of  $\rho_\ell$  depend on the type of underlying perturbations and cosmological background model.

The complex pdf (17) with  $m \neq 0$  is equivalent to the product of joint pdf's for real and imaginary parts of  $(a_{\ell m}^T, a_{\ell m}^E)$ , i.e. for  $(a_{\ell m}^{T(r)}, a_{\ell m}^{E(r)})$  and  $(a_{\ell m}^{T(i)}, a_{\ell m}^{E(i)})$  with  $\ell \geq m \geq 1$  [5]. Introducing the label  $c = r$  or  $i$  one can write the common formula

$$f(a_{\ell m}^{T(c)}, a_{\ell m}^{E(c)}) = \frac{1}{\pi\sigma_\ell^T\sigma_\ell^E\sqrt{1-\rho_\ell^2}} \exp\left\{-\frac{1}{(1-\rho_\ell^2)}\left[\frac{(a_{\ell m}^{T(c)})^2}{(\sigma_\ell^T)^2} + \frac{(a_{\ell m}^{E(c)})^2}{(\sigma_\ell^E)^2} - \frac{2\rho_\ell a_{\ell m}^{T(c)} a_{\ell m}^{E(c)}}{\sigma_\ell^T\sigma_\ell^E}\right]\right\}. \quad (20)$$

The quantities  $\{\sigma_\ell^T, \sigma_\ell^E, \sigma_\ell^B, \rho_\ell\}$  participating and defining the pdf's are related with the CMB power spectra calculated in Sec. III B:

$$(\sigma_\ell^T)^2 = C_\ell^{TT}, \quad (\sigma_\ell^E)^2 = C_\ell^{EE}, \quad (\sigma_\ell^B)^2 = C_\ell^{BB}, \quad \rho_\ell\sigma_\ell^T\sigma_\ell^E = C_\ell^{TE}. \quad (21)$$

We will use these relations in our further discussion.

#### IV. ESTIMATORS OF THE CMB POWER SPECTRA AND THEIR PROBABILITY DENSITY FUNCTIONS

The quantum-mechanical origin of cosmological perturbations, which we represented by randomness of  $\hat{c}_\mathbf{n}$ , does not allow one to predict a unique CMB map, i.e. one concrete set of multipole coefficients  $a_{\ell m}^X$ . The most that theory allows is to formulate probability density functions, and we have done this. The pdf's are fully characterized by the set of numbers  $\{\sigma_\ell^T, \sigma_\ell^E, \sigma_\ell^B, \rho_\ell\}$  or, equivalently, by the power spectra (21). Theory can predict these parameters, while observations can check whether these parameters are indeed as predicted.

To find a parameter from observations, one normally uses an appropriate random variable (statistic) called an estimator. The estimator is unbiased if its mean value is equal to the parameter, and best if its variance is as small as possible. A concrete value of the estimator calculated on the actually observed data (in our case, on the set of actually observed multipole coefficients  $a_{\ell m}^X$ ) gives an estimate of the parameter. We will denote by symbol  $D_\ell^{XX'}$  the best unbiased estimators of the power spectra  $C_\ell^{XX'}$  and will consider separately the auto-correlation,  $X = X'$ , and cross-correlation,  $XX' = TE$ , estimators.

##### A. Estimators of the auto-correlation power spectra

It is clear from Eq. (10) that there exists plenty of unbiased estimators of  $C_\ell^{XX}$ . Each of  $2\ell + 1$  estimators (random variables)  $(a_{\ell m}^X a_{\ell m}^{X*})$  with  $\ell \geq m \geq -\ell$  calculated on the observed multipoles provides an unbiased estimate of  $C_\ell^{XX}$ . However, there exists only one best unbiased estimator. It is given by

$$D_\ell^{XX} = \frac{1}{2\ell + 1} \sum_{m=-\ell}^{\ell} (a_{\ell m}^X a_{\ell m}^{X*}).$$

The expectation value of this estimator is, as required,

$$\langle D_\ell^{XX} \rangle = \frac{1}{2\ell+1} \sum_{m=-\ell}^{\ell} \langle a_{\ell m}^X a_{\ell m}^{X*} \rangle = (\sigma_\ell^X)^2 = C_\ell^{XX}. \quad (22)$$

The standard deviation is  $\Delta D_\ell^{XX} \equiv \sqrt{\langle (D_\ell^{XX})^2 \rangle - \langle D_\ell^{XX} \rangle^2}$ , amounts to [29], [8], [30]

$$\Delta D_\ell^{XX} = (\sigma_\ell^X)^2 \sqrt{\frac{2}{2\ell+1}}. \quad (23)$$

This is the smallest, but still a non-zero, variance among all possible quadratic estimators [30]. (Formula (23) provides one of interpretations of the term ‘cosmic variance’.)

We have access to only one realization of the inherently random CMB field, that is, we can deal with only one observed set of multipole coefficients  $a_{\ell m}^X$ . Under certain conditions, the access to only one realization of the stochastic process is sufficient for extraction the true parameters of the process, with probability arbitrarily close to 1, from the data. When this is possible the stochastic process is called ergodic. However, there is no ergodic processes on a 2-sphere (our sky) [30]. We will always be facing some uncertainty surrounding the parameters extracted from the observed CMB field.

The variance of an estimator at each  $\ell$  is just a number, and is not sufficient for proper handling of the data. The full available information is contained in the pdf of the estimator. In order to derive the pdf of  $D_\ell^{XX}$ , ( $XX = TT, EE, BB$ ), we will first rewrite it as

$$D_\ell^{XX} = \frac{2}{2\ell+1} \left( \left( \frac{a_{\ell 0}^{X(r)}}{\sqrt{2}} \right)^2 + \sum_{m=1}^{\ell} [(a_{\ell m}^{X(r)})^2 + (a_{\ell m}^{X(i)})^2] \right), \quad (m \geq 1).$$

It is clear that the estimator  $D_\ell^{XX}$  is just the sum of squares of  $(2\ell+1)$  independent normal variables. Thus, for every fixed  $\ell$ , the estimator obeys a  $\chi^2$  distribution with  $2\ell+1$  degrees of freedom [5].

In what follows, Sec. VI B, we will be dealing with the problem of observations on a cut sky. The cut sky limitation effectively means that, for a given  $\ell$ , one has access not to all  $2\ell+1$  degrees of freedom, but only to a smaller number  $n$ ,  $n = (2\ell+1)f_{\text{sky}}$ , where  $f_{\text{sky}}$  is the observed fraction of the sky [31, 32, 33]. In preparation to this problem, we are writing down the pdf for  $D_\ell^{XX}$  with  $n$  degrees of freedom,  $D_\ell^{XX}(n)$ , where  $n$  is not necessarily equal to  $2\ell+1$ . Denoting  $V \equiv nD_\ell^{XX}(n)/(\sigma_\ell^X)^2$ , one writes [5]

$$f(D_\ell^{XX}(n)) = \frac{nV^{n/2-1}e^{-V/2}}{2^{n/2}\Gamma(n/2)(\sigma_\ell^X)^2}, \quad (24)$$

where  $\Gamma$  is the *Gamma*-function. Certainly, when  $n = 2\ell+1$ , the mean value and the standard deviation of the variable  $D_\ell^{XX}$  derivable from the pdf (24), coincide with the already written expressions (22) and (23).

## B. Estimators of the cross-correlation $TE$ power spectrum

The  $TE$  cross-correlation is in the focus of this paper, so we shall explore the  $TE$  estimator in depth, without sparing details. We know that the  $C_\ell^{TE}$  correlation function should be positive, if caused by density perturbations, from  $\ell = 2$  and up to  $\ell \approx 53$ ; and it should be negative, if caused by gravitational waves, from  $\ell = 2$  and up to  $\ell \approx 150$  [3], a further study of the  $TE$  correlation was conducted in [34]. But  $C_\ell^{TE}$  is only the mean value of the correlations. In a particular realization of the random field, i.e. for the actually observed  $a_{\ell m}^X$ , the  $D_\ell^{TE}$  outcomes can be negative, despite the fact that the theoretical  $C_\ell^{TE}$  is positive, and vice versa. Suppose negative correlations are observed in a set of multipoles. Is it necessarily a signature of gravitational waves, or it may be a statistical fluke of density perturbations alone? Suppose positive correlations are observed in a set of multipoles. Are they ‘positive enough’ to be explained by density perturbations alone, or they require an admixture of gravitational waves? This is the kind of fundamental questions of the  $TE$  approach that we need to answer [2], and they can only be answered on the basis of the probability density functions for the estimators.

It is clear from the previous discussion and Eq. (12) that the best unbiased estimator  $D_\ell^{TE}$  is given by

$$D_\ell^{TE} \equiv \frac{1}{2(2\ell+1)} \sum_{m=-\ell}^{\ell} (a_{\ell m}^T a_{\ell m}^{E*} + a_{\ell m}^{T*} a_{\ell m}^E).$$

It can also be written as

$$D_\ell^{TE} = \frac{1}{2\ell+1} \left( v_{\ell 0}^{(r)} + \sum_{m=1}^{\ell} (v_{\ell m}^{(r)} + v_{\ell m}^{(i)}) \right) \quad (25)$$

where

$$v_{\ell 0}^{(r)} \equiv a_{\ell 0}^{T(r)} a_{\ell 0}^{E(r)}, \quad v_{\ell m}^{(r)} \equiv 2a_{\ell m}^{T(r)} a_{\ell m}^{E(r)}, \quad v_{\ell m}^{(i)} \equiv 2a_{\ell m}^{T(i)} a_{\ell m}^{E(i)}, \quad (m \geq 1). \quad (26)$$

As before, we denote quantities (26) by  $v_{\ell m}^{(c)}$ , where  $c = r$  or  $i$ ,  $m \geq 0$ . Obviously, as the coefficients  $a_{\ell 0}^T, a_{\ell 0}^E$  are real,  $v_{\ell 0}^{(i)} = 0$ .

Each of the quantities  $v_{\ell m}^{(c)}$  is an unbiased (but not the best) estimator of  $C_\ell^{TE}$ , as follows from the averages based on the joint pdf (20):

$$\langle v_{\ell m}^{(c)} \rangle = \rho_\ell \sigma_\ell^T \sigma_\ell^E = C_\ell^{TE}, \quad \Delta v_{\ell m}^{(c)} = \sqrt{1 + \rho_\ell^2 \sigma_\ell^T \sigma_\ell^E} = \sqrt{C_\ell^{TT} C_\ell^{EE} + (C_\ell^{TE})^2}.$$

In order to analyze the pdf of the estimator  $D_\ell^{TE}$  in (25), it is instructive to study in the pdf for quantities  $v_{\ell m}^{(c)}$ . In Appendix A we present a detailed discussion of these pdfs and some of their relevant properties.

Based on the above analysis and the results from Appendix A, we are now in the position to derive the pdf for the best unbiased estimator  $D_\ell^{TE}$ . Firstly, the mean value and the standard deviation of  $D_\ell^{TE}$  are known from the joint  $TE$  pdf:

$$\langle D_\ell^{TE} \rangle = \frac{1}{2(2\ell+1)} \sum_{m=-\ell}^{\ell} \langle a_{\ell m}^T a_{\ell m}^{E*} + a_{\ell m}^{T*} a_{\ell m}^E \rangle = \rho_\ell \sigma_\ell^T \sigma_\ell^E = C_\ell^{TE}, \quad (27)$$

$$\Delta D_\ell^{TE} \equiv \sqrt{\langle (D_\ell^{TE})^2 \rangle - \langle D_\ell^{TE} \rangle^2} = \sigma_\ell^T \sigma_\ell^E \sqrt{\frac{\rho_\ell^2 + 1}{2\ell+1}} = \sqrt{\frac{C_\ell^{TT} C_\ell^{EE} + (C_\ell^{TE})^2}{2\ell+1}} = \frac{\Delta v_{\ell m}^{(c)}}{\sqrt{2\ell+1}}. \quad (28)$$

Clearly,  $\Delta D_\ell^{TE}$  is smaller than  $\Delta v_{\ell m}^{(c)}$  by a factor  $\sqrt{2\ell+1}$ . The minimum of  $\Delta D_\ell^{TE}$  is at  $\rho_\ell = 0$  and the maximum is at  $|\rho_\ell| = 1$ . The maximum is only  $\sqrt{2}$  times greater than the minimum. For growing  $\ell$  and fixed  $\sigma_\ell^T, \sigma_\ell^E, \rho_\ell$ , the standard deviation is decreasing as  $1/\sqrt{2\ell+1}$ .

To derive the pdf  $f(D_\ell^{TE})$  one notes (see Eq. (25)) that the variable  $D_\ell^{TE}$  is essentially the sum of  $2\ell+1$  products of normally distributed variables from two classes,  $T$  and  $E$ , with standard deviations  $\sigma_\ell^T$  and  $\sigma_\ell^E$ , respectively. Since we will be interested in the situation where the number  $n$  of accessible degrees of freedom is smaller than  $2\ell+1$ , we have to make the derivation more general. It is instructive to start from a somewhat abstract problem.

Let the three variables  $x, y, z$  be defined by

$$x \equiv X_1^2 + X_2^2 + \dots + X_n^2, \quad y \equiv Y_1^2 + Y_2^2 + \dots + Y_n^2, \quad z \equiv X_1 Y_1 + X_2 Y_2 + \dots + X_n Y_n, \quad (29)$$

where  $X_i$  and  $Y_i$  ( $1 \leq i \leq n$ ) are real variables. We assume that within each class,  $X$  and  $Y$ , the variables are statistically independent and each  $X_i$  and  $Y_i$  obeys a zero-mean normal distribution with standard deviation  $\sigma^X$  and  $\sigma^Y$ , respectively. We also assume that each pair  $X_i, Y_i$  obeys a zero-mean bivariate normal distribution with correlation coefficient  $\rho$ . Then, the joint pdf  $f(x, y, z)$  is a Wishart distribution with  $n$  degrees of freedom [5]:

$$f(x, y, z) = \left( \frac{1}{4(1-\rho^2)(\sigma^X \sigma^Y)^2} \right)^{n/2} \frac{(xy - z^2)^{\frac{n-3}{2}}}{\pi^{1/2} \Gamma(\frac{n}{2}) \Gamma(\frac{n-1}{2})} \\ \times \exp \left\{ -\frac{1}{2(1-\rho^2)} \left( \frac{x}{(\sigma^X)^2} + \frac{y}{(\sigma^Y)^2} - \frac{2\rho z}{\sigma^X \sigma^Y} \right) \right\}.$$

From this distribution, by integrating over variables  $x$  and  $y$ , one derives the pdf  $f(z)$ :

$$f(z) = \sqrt{\frac{|z|^{n-1}}{2^{n-1} \pi (\sigma^X \sigma^Y)^{n+1} (1-\rho^2)}} \frac{1}{\Gamma(\frac{n}{2})} \exp \left\{ \frac{\rho}{1-\rho^2} \frac{z}{\sigma^X \sigma^Y} \right\} K_{\frac{n-1}{2}} \left( \frac{|z|}{(1-\rho^2) \sigma^X \sigma^Y} \right), \quad (30)$$

where  $K_{\frac{n-1}{2}}$  is the  $(\frac{n-1}{2})$ -order modified Bessel function. In this derivation we have used (2.382.2) and (3.471.9) from Ref. [35]. In the special case  $n = 1$ , and denoting the pair  $X_1, Y_1$  by  $a_{\ell 0}^T, a_{\ell 0}^E$  or  $\sqrt{2}a_{\ell m}^{T(c)}, \sqrt{2}a_{\ell m}^{E(c)}$ , (for fixed  $m \geq 1$ ,  $c = r$  or  $i$ ), one finds that the pdf (30) returns to the pdf (A1) for each  $v_{\ell m}^{(c)}$ .

The pdf for the estimator  $D_\ell^{TE}(n)$  with  $n$  degrees of freedom, where  $n$  is not necessarily equal to  $2\ell + 1$ , follows now from Eq. (30). Comparing Eqs. (25, 29) we write  $D_\ell^{TE}(n) = z/n$  and, then, the pdf for  $D_\ell^{TE}(n)$  (omitting argument  $n$ ):

$$f(D_\ell^{TE}) = \left(\frac{|D_\ell^{TE}|}{2}\right)^{\frac{n-1}{2}} \left(\frac{n}{\sigma_\ell^T \sigma_\ell^E}\right)^{\frac{n+1}{2}} \sqrt{\frac{1}{\pi(1-\rho_\ell^2)} \frac{1}{\Gamma(\frac{n}{2})}} \\ \times \exp\left\{\frac{\rho_\ell}{1-\rho_\ell^2} \frac{n D_\ell^{TE}}{\sigma_\ell^T \sigma_\ell^E}\right\} K_{\frac{n-1}{2}}\left(\frac{n|D_\ell^{TE}|}{(1-\rho_\ell^2)\sigma_\ell^T \sigma_\ell^E}\right). \quad (31)$$

Certainly, Eqs. (27, 28) are consequences of this pdf, when  $n = 2\ell + 1$ . In Appendix B we discuss some useful properties of this pdf. These properties are used in our consequent analysis, in particular for determining the confidence intervals of  $D_\ell^{TE}$  for specific cosmological models.

## V. CORRELATION COEFFICIENT $\rho_\ell$ AND ESTIMATOR $D_\ell^{TE}$ IN SPECIFIC MODELS

The sign and value of the  $TE$  correlations, as well as their statistical distribution, crucially depend on the sign and value of the correlation coefficient  $\rho_\ell$ . As we know, at lower  $\ell$ 's,  $\rho_\ell$  should be negative for gravitational waves and positive for density perturbations. However, specific numerical values of  $\rho_\ell$  are different in different models. It is difficult to find  $\rho_\ell$  analytically, so we are using numerical calculations to find it numerically.

### A. Numerical evaluation of the correlation coefficient $\rho_\ell$

Assuming that the correlation functions  $C_\ell^{TT}, C_\ell^{EE}, C_\ell^{TE}$  are known from numerical modelling, the  $\rho_\ell$  can be found from the defining expressions (19), (15):

$$\rho_\ell = \frac{C_\ell^{TE}}{\sqrt{C_\ell^{TT} C_\ell^{EE}}} = \frac{C_\ell^{TE}(dp) + C_\ell^{TE}(gw)}{\sqrt{(C_\ell^{TT}(dp) + C_\ell^{TT}(gw))(C_\ell^{EE}(dp) + C_\ell^{EE}(gw))}}. \quad (32)$$

In our numerical calculations we work with a single cosmological background model, which is the ‘best-fit’  $\Lambda$ CDM cosmology based on the 5-year WMAP observations and other data sets [4]. The parameters of the background model are

$$\Omega_b h^2 = 0.02265 \pm 0.00059, \quad \Omega_c h^2 = 0.1143 \pm 0.0034, \\ \Omega_\Lambda = 0.721 \pm 0.015, \quad \tau_{reion} = 0.084 \pm 0.016. \quad (33)$$

The associated value of the Hubble parameter is  $h = 0.701 \pm 0.013$ . In calculations, we are using the central values of these parameters.

As for the perturbations, the WMAP5 ‘best-fit’ analysis suggests no contribution from gravitational waves, whereas density perturbations are characterized by the spectral index  $n_s$  and the amplitude  $\Delta_{\mathcal{R}}^2$  [4, 36]:

$$n_s = 0.960_{-0.013}^{+0.014}, \quad \Delta_{\mathcal{R}}^2 = (2.457_{-0.093}^{+0.092}) \times 10^{-9}, \quad (\text{at } k = 0.002 \text{Mpc}^{-1}). \quad (34)$$

The WMAP5 ‘best-fit’ parameters (33), (34) imply the temperature quadrupole

$$\frac{\ell(\ell+1)C_{\ell=2}^{TT}}{2\pi} = 1160 \text{ } (\mu\text{K}^2). \quad (35)$$

Being guided by the quantum-mechanical theory of cosmological perturbations (see Sec. I), we include gravitational waves in our analysis from the very beginning, as a necessary ingredient of CMB anisotropies at lower  $\ell$ 's. We allow the  $dp$  parameters (34) to vary and strive to achieve the total theoretical  $TT, EE, TE$  spectra as close as possible to the observed data. Gravitational waves are parameterized by the primordial spectral index  $n_t$ , where  $n_t = n_s - 1$

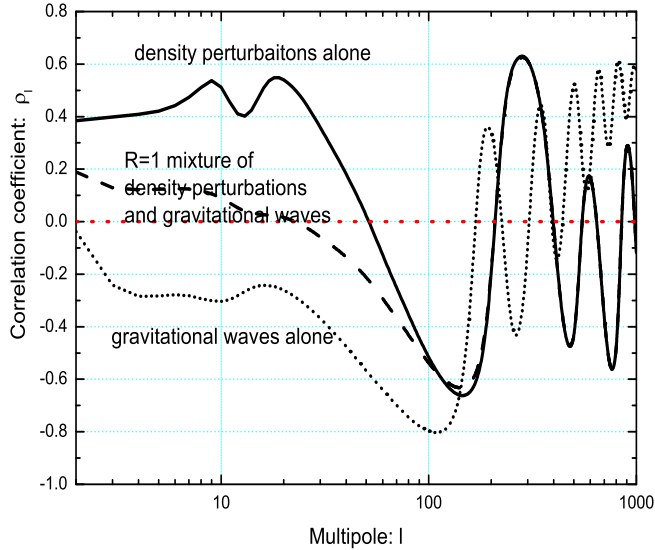


FIG. 1: The correlation coefficient  $\rho_\ell$  as a function of  $\ell$  in models with different amounts of gravitational waves. The solid line denotes the best-fit  $\Lambda$ CDM model with density perturbation alone, the dashed line is for the  $R = 1$  mixture of  $dp$  and  $gw$ , and the dotted line is for gravitational waves alone.

(unless some other  $n_t$  is chosen for purposes of illustration), and the amplitude parameter  $R$ , where  $R$  is the ratio of the  $gw$  and  $dp$  contributions to the temperature quadrupole:

$$R \equiv \frac{C_{\ell=2}^{TT}(gw)}{C_{\ell=2}^{TT}(dp)}. \quad (36)$$

To avoid any ambiguities in definitions and derived upper limits, we do not use the ‘tensor-to-scalar ratio’ parameter  $r$  (see [2]). For very rough comparison of results, one can keep in mind the approximate relationship  $r \simeq 2R$ , which follows from the study [37]. In power spectra calculations we rely on the CMBFast code [38] (Alternatively one can use the CAMB [39] which gives consistent results). The correlation coefficient  $\rho_\ell$  is then found from Eq. (32).

In the way of illustration, we plot in Fig. 1 the  $\rho_\ell$  for three representative sets of perturbations on the background of  $\Lambda$ CDM cosmology (33). The solid curve shows  $\rho_\ell$  for density perturbations alone with best-fit parameters (34). The dotted curve is for  $\rho_\ell$  when gravitational waves alone are present with  $n_t = 0$  and the amplitude normalization such that the temperature quadrupole is equal to the best-fit WMAP5 prediction (35). The dashed curve shows  $\rho_\ell$  arising in the  $R = 1$  mixture of density perturbations ( $n_s = 0.96$ ) and gravitational waves ( $n_t = 0$ ) with total quadrupole equal to the WMAP5 best-fit value (35).

As expected [3] and seen in Fig. 1,  $\rho_\ell$  is positive for  $dp$  and negative for  $gw$  at lower multipoles,  $\ell \lesssim 50$ . In the intermediate case  $R = 1$ ,  $\rho_\ell$  is small  $|\rho_\ell| < 0.2$ , as the  $dp$  and  $gw$  contributions largely cancel each other. At higher multipoles,  $\ell > 100$ , the  $R = 1$  curve approaches the  $dp$  curve, as the role of gravitational waves diminishes in comparison with density perturbations [3, 40]. The oscillatory features at very low multipoles  $\ell \sim 10 - 20$  (clearly seen in the solid curve) are real. They are a reflection of effects of  $\Omega_\Lambda$  in combination with the reionization era characterized by the optical depth  $\tau_{reion}$ .

Knowing  $\rho_\ell$  as a function of  $\ell$  one can build and analyse pdf’s for the  $D_\ell^{TE}$  estimator in specific models. As we show below, the sign difference in  $\rho_\ell$ ’s for density perturbations and gravitational waves is crucial for telling one sort of perturbations from another.

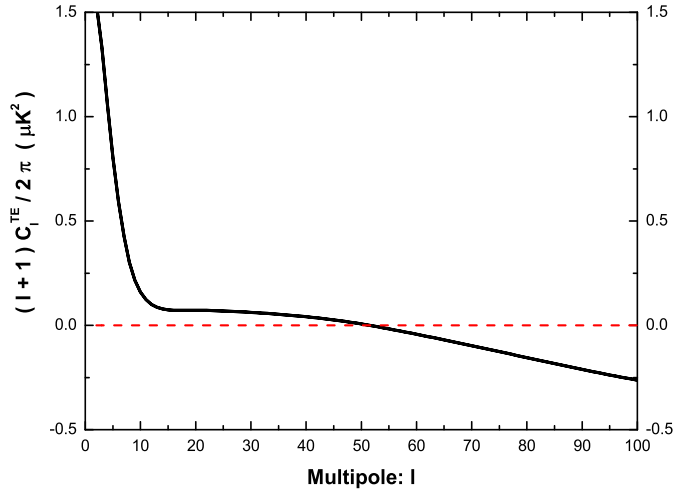


FIG. 2: The  $(\ell + 1)C_\ell^{TE}/2\pi$  power spectrum in units of  $(\mu\text{K}^2)$  for the best-fit WMAP5 model with no gravitational waves.

### B. Probability of negative values of the estimator $D_\ell^{TE}$

In the center of our attention is the WMAP5 best-fit model (33), (34) with no gravitational waves,  $R = 0$ . The mean value of the estimator  $D_\ell^{TE}$ , i.e. the  $TE$  power spectrum, is shown in Fig. 2. To assess the consistency of this graph with the actually observed data points [4, 41] (see also [42]), many of which are negative at  $\ell \lesssim 50$ , we start from the pdf for this model. We first ignore noises and systematic effects, but will take them into account in Sec. VI.

Our derivation is based on Eq. (31), with  $n = 2\ell + 1$ , and  $\rho_\ell$ , as plotted by solid line in Fig. 1. In Fig. 3 we show  $f(D_\ell^{TE})$  for a series of multipoles,  $\ell = 2, 10, 20, 30, 50, 100$ . When  $\ell$  increases, maxima of individual pdf's move from positive to negative values, crossing zero at  $\ell \approx 53$ , in agreement with Fig. 2. The spread of individual pdf's becomes narrower with increasing  $\ell$  (note increasing horizontal scale on different panels), in agreement with the decreasing standard deviation  $\Delta D_\ell^{TE} \propto \sigma_\ell^T \sigma_\ell^E / \sqrt{(2\ell + 1)}$ , as reflected in (28). We also plot by dashed curves the Gaussian approximation to the exact pdf's,

$$f_G(D_\ell^{TE}) = \frac{1}{\sqrt{2\pi}\Delta D_\ell^{TE}} \exp\left[-\frac{(D_\ell^{TE} - C_\ell^{TE})^2}{2(\Delta D_\ell^{TE})^2}\right]. \quad (37)$$

As could be anticipated, the Gaussian approximation becomes progressively better with the increasing  $\ell$ .

We shall now draw various confidence intervals surrounding the mean value at each  $\ell$ . The confidence regions are determined by the shortest interval between the upper  $(D_\ell^{TE})_U$  and the lower  $(D_\ell^{TE})_L$  boundaries enclosing a given surface area under the pdf, as discussed in Appendix A.

In Fig. 4, we draw confidence intervals for all three models considered in Fig. 1. Namely, the best-fit model with density perturbations alone (left panel), the  $R = 1$  mixture of density perturbations and gravitational waves (middle panel), and a model with gravitational waves alone (right panel). It is seen on the left panel that the 99.7% confidence region is above the zero line for  $15 \lesssim \ell \lesssim 29$ . The 95.4% confidence region is above the zero line for  $\ell < 37$ , while the 68.3% confidence region lies in the positive territory for all  $\ell < 45$ . In contrast, the right panel for gravitational waves alone shows that all plotted confidence regions are well below the zero line for  $\ell \gtrsim 25$ .

Finally, in Fig. 5, we show the probability  $P(D_\ell^{TE} < 0)$  of finding negative data points in models with varying amounts of density perturbations and gravitational waves. In all combinations of  $dp$  and  $gw$ , the spectral indices are  $n_s = 0.96$ ,  $n_t = 0$  and the total quadrupole is equal to the best-fit value (35). The black solid curve is for the WMAP5 best-fit model with no gravitational waves,  $R = 0$ . It is seen from the graph that in the case of density perturbations alone, the probability  $P(D_\ell^{TE} < 0)$  is pretty small, especially in the range of multipoles  $10 < \ell < 30$ . The lowest

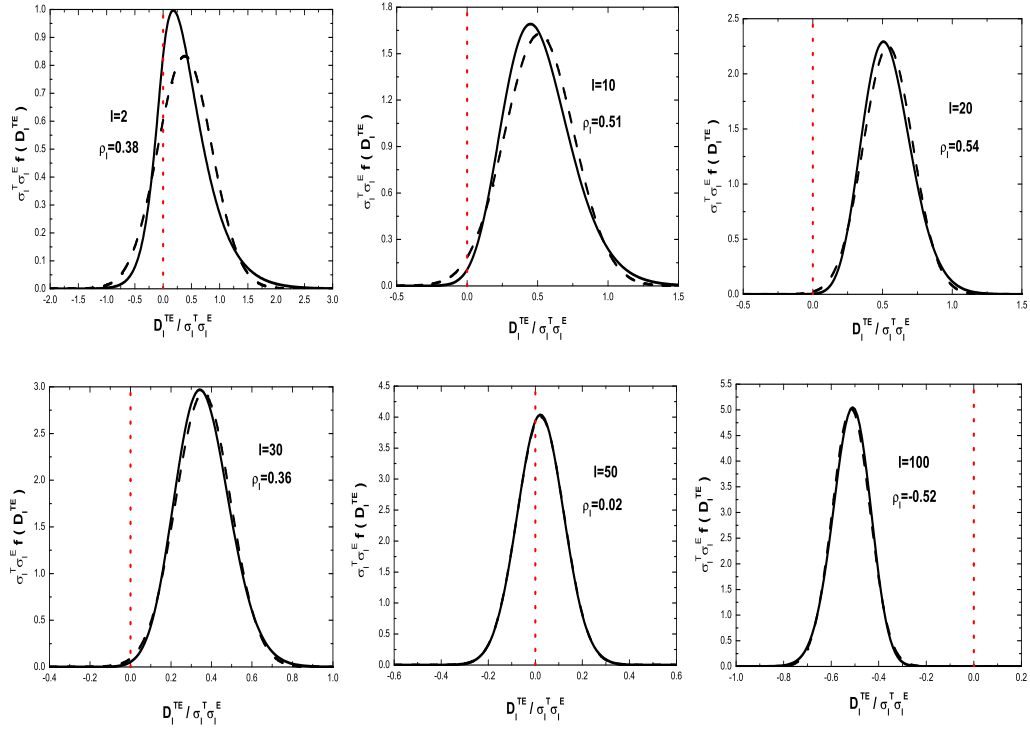


FIG. 3: Probability density functions  $f(D_\ell^{TE})$  at  $\ell = 2, 10, 20, 30, 50, 100$  for the WMAP5 best-fit model (33), (34). The dashed curves show the Gaussian approximation to the exact pdf's.

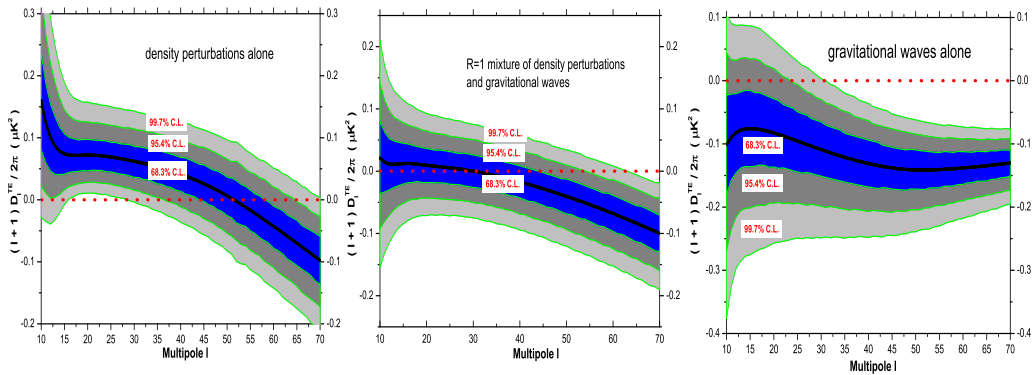


FIG. 4: The 68.3%, 95.4%, 99.7% confidence intervals of the variable  $D_\ell^{TE}$  for three representative models shown in Fig. 1. In all three panels, the solid black curves are the mean values of the statistic  $(\ell+1)D_\ell^{TE}/2\pi$ , i.e. the power spectra  $(\ell+1)C_\ell^{TE}/2\pi$ .

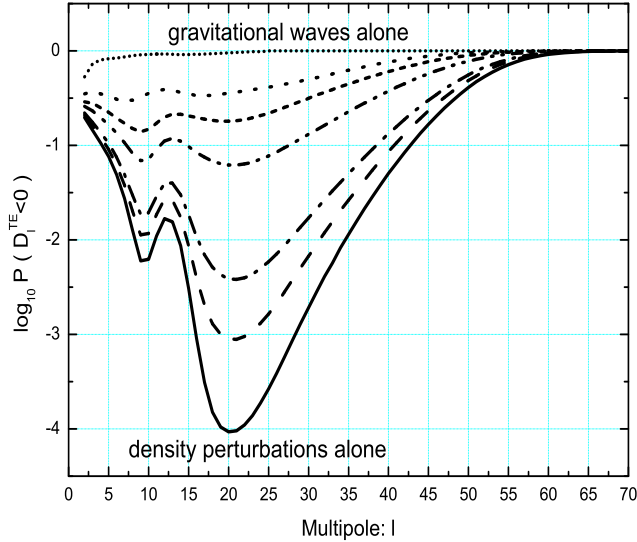


FIG. 5: The probability of finding negative  $TE$  data points in different models. The curves are ordered from the bottom to the top by increasing  $R$ ,  $R = 0.0, 0.05, 0.1, 0.3, 0.5, 1.0$  with  $gw$  alone at the very top.

point is at  $\ell = 20$ , with  $P(D_{\ell=20}^{TE} < 0) = 9.33 \times 10^{-5}$ . Obviously, when the amount of gravitational waves increases, the  $P(D_{\ell}^{TE} < 0)$  approaches 1.

## VI. NOISES AND OTHER SOURCES OF INCREASED UNCERTAINTY

The spread of the probability density functions discussed so far is the unavoidable consequence of the inherent randomness of the sought after signal  $a_{\ell m}^X$ . Additional randomness, and additional uncertainty in the parameter estimation, is brought in by the process of measurement. The output (observed) readings are contaminated by instrumental noises and various foreground radiations, such as the synchrotron radiation, thermal emission from dust, unresolved extragalactic sources, etc. [29, 43, 44, 45, 46, 47, 48]. It is common to treat the residual systematic causes as ‘effective noises’ alongside with the ‘genuine’ instrumental noises. In addition, the incomplete sky coverage and the sky map cuts [31, 32, 33, 49] introduce extra loss of information in comparison to what is available on the full sky. It is common to treat this complication by a proper reduction of the potentially available  $2\ell + 1$  degrees of freedom at each  $\ell$ .

We shall now see how these factors expand the confidence intervals of various estimators, and in particular the  $D_{\ell}^{TE}$ . Only by taking all these factors into account, we will be in the position to test the ‘null’ (no gravitational waves) hypothesis (33), (34), and make predictions for the forthcoming experiments.

### A. Effects of noises

In general, the multipole coefficients  $a_{\ell m}^X(o)$  observed in a CMB measurement consist of a signal convolved with the beam window function,  $a_{\ell m}^X(s)W_{\ell}$ , and a collective noise contribution  $a_{\ell m}^X(n)$ :

$$a_{\ell m}^X(o) = a_{\ell m}^X(s)W_{\ell} + a_{\ell m}^X(n).$$

For WMAP and Planck satellites, the window function  $W_{\ell}$  is close to 1 at  $\ell \lesssim 100$  [43, 44], so we set  $W_{\ell} = 1$ .



As usual [29, 49, 50, 51], we assume that the noise terms  $a_{\ell m}^X(n)$  and the signal terms  $a_{\ell m}^X(s)$  are statistically independent of each other. Also, any two members in the set  $\{a_{\ell m}^X(n)|X = T, E, B; \ell = 2, 3, \dots; m = -\ell, \dots, \ell\}$  are statistically independent, while each member  $a_{\ell m}^X(n)$  obeys a normal distribution with zero mean and standard deviation  $\sigma_\ell^X(n)$ ,

$$\langle a_{\ell m}^X(n)a_{\ell m}^{X*}(n) \rangle = (\sigma_\ell^X(n))^2 = N_\ell^{XX}.$$

It is presumed that the noise power spectra  $N_\ell^{XX}$  are known from independent evaluations. Obviously, the  $TE$  noise power spectrum vanishes,  $N_\ell^{TE} = 0$ , due to the absence of correlations between  $a_{\ell m}^T(n)$  and  $a_{\ell m}^E(n)$ .

1. *Probability density functions for multipole coefficients  $a_{\ell m}^X(o)$  and estimators  $D_\ell^{XX'}(o)$*

Since  $a_{\ell m}^X(s)$  and  $a_{\ell m}^X(n)$  are statistically independent and obey zero-mean normal distributions, their sum  $a_{\ell m}^X(o)$  obeys a zero-mean normal distribution with the variance  $(\sigma_\ell^X(o))^2$ , which is the sum of the signal and noise variances,

$$(\sigma_\ell^X(o))^2 = \langle a_{\ell m}^X(o)a_{\ell m}^{X*}(o) \rangle = \langle a_{\ell m}^X(s)a_{\ell m}^{X*}(s) \rangle + \langle a_{\ell m}^X(n)a_{\ell m}^{X*}(n) \rangle = C_\ell^{XX} + N_\ell^{XX}.$$

The joint pdf  $f(a_{\ell m}^T(o), a_{\ell m}^E(o))$  is a zero-mean bivariate normal distribution with the correlation coefficient  $\rho_\ell(o)$ ,

$$\rho_\ell(o) = \frac{\frac{1}{2}\langle a_{\ell m}^T(o)a_{\ell m}^{E*}(o) + a_{\ell m}^{T*}(o)a_{\ell m}^E(o) \rangle}{\sqrt{\langle a_{\ell m}^T(o)a_{\ell m}^{T*}(o) \rangle \langle a_{\ell m}^E(o)a_{\ell m}^{E*}(o) \rangle}} = \frac{C_\ell^{TE}}{\sqrt{(C_\ell^{TT} + N_\ell^{TT})(C_\ell^{EE} + N_\ell^{EE})}}. \quad (38)$$

Comparing Eq. (38) with Eq. (19) one finds that the noises make the output correlation coefficient  $\rho_\ell(o)$  smaller than the no-noise correlation coefficient  $\rho_\ell$ .

The unbiased auto-correlation estimators in the presence of noise are defined by

$$D_\ell^{XX}(o) = \frac{1}{2\ell+1} \sum_{m=-\ell}^{\ell} (a_{\ell m}^X(o)a_{\ell m}^{X*}(o)) - N_\ell^{XX}.$$

The expectation value and the standard deviation amount to

$$\begin{aligned} \langle D_\ell^{XX}(o) \rangle &= (\sigma_\ell^X(o))^2 - N_\ell^{XX} = C_\ell^{XX}, \\ \Delta D_\ell^{XX}(o) &= \sqrt{\frac{2}{2\ell+1}(\sigma_\ell^X(o))^2} = \sqrt{\frac{2}{2\ell+1}(C_\ell^{XX} + N_\ell^{XX})}. \end{aligned} \quad (39)$$

Comparing with Eq. (23) one finds that the noises make the standard deviation  $\Delta D_\ell^{XX}(o)$  larger than the no-noise value  $\Delta D_\ell^{XX}$ .

The pdf of the estimator  $D_\ell^{XX}(o)$  with  $n$  degrees of freedom can be derived in a way similar to that in Sec. IV A,

$$f(D_\ell^{XX}(o)) = \frac{n(V(o))^{n/2-1}e^{-V(o)/2}}{2^{n/2}\Gamma(n/2)(\sigma_\ell^X(o))^2},$$

where  $V(o) \equiv n(D_\ell^{XX}(o) + N_\ell^{XX})/(\sigma_\ell^X(o))^2$ .

Finally, we have to consider the unbiased cross-correlation estimator  $D_\ell^{TE}(o)$  which is of prime importance for us,

$$D_\ell^{TE}(o) = \frac{1}{2(2\ell+1)} \sum_{m=-\ell}^{\ell} (a_{\ell m}^T(o)a_{\ell m}^{E*}(o) + a_{\ell m}^{T*}(o)a_{\ell m}^E(o)).$$

The expectation value and the standard deviation amount to

$$\begin{aligned} \langle D_\ell^{TE}(o) \rangle &= \rho_\ell(o)\sigma_\ell^T(o)\sigma_\ell^E(o) = C_\ell^{TE}, \\ \Delta D_\ell^{TE}(o) &= \sqrt{\frac{(\rho_\ell(o))^2+1}{2\ell+1}\sigma_\ell^T(o)\sigma_\ell^E(o)} = \sqrt{\frac{(C_\ell^{TT}+N_\ell^{TT})(C_\ell^{EE}+N_\ell^{EE})+(C_\ell^{TE})^2}{2\ell+1}}. \end{aligned} \quad (40)$$

Again, the noises make the standard deviation swell in comparison with the no-noise case (28).

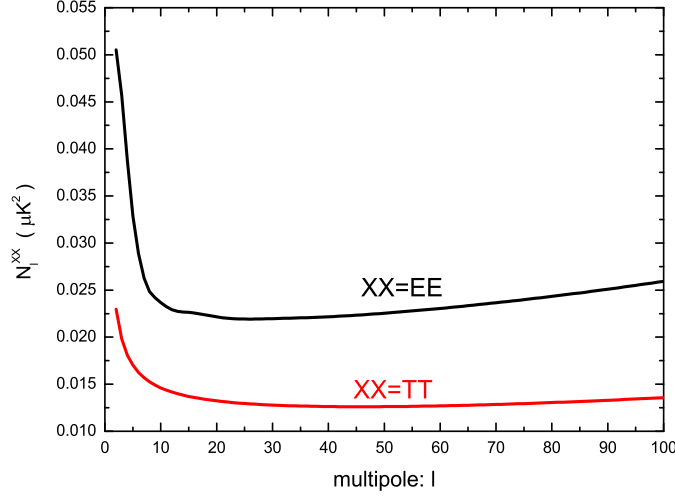


FIG. 6: The estimation of the WMAP5 noises  $N_\ell^{TT}$  and  $N_\ell^{EE}$ .

The pdf for the estimator  $D_\ell^{TE}(o)$  with  $n$  degree of freedom is similar to that in Sec. IV B,

$$f(D_\ell^{TE}(o)) = \left( \frac{|D_\ell^{TE}(o)|}{2} \right)^{\frac{n-1}{2}} \left( \frac{n}{\sigma_\ell^T(o)\sigma_\ell^E(o)} \right)^{\frac{n+1}{2}} \sqrt{\frac{1}{\pi(1-(\rho_\ell(o))^2)} \frac{1}{\Gamma(\frac{n}{2})}} \\ \times \exp \left\{ \frac{\rho_\ell(o)}{1-(\rho_\ell(o))^2} \frac{nD_\ell^{TE}(o)}{\sigma_\ell^T(o)\sigma_\ell^E(o)} \right\} K_{\frac{n-1}{2}} \left[ \frac{n|D_\ell^{TE}(o)|}{(1-(\rho_\ell(o))^2)\sigma_\ell^T(o)\sigma_\ell^E(o)} \right]. \quad (41)$$

To summarize, the pdf (41), which includes noises, retains the functional form of the no-noise pdf (31), but with the anticipated substitutions. Namely,  $D_\ell^{TE}$ ,  $\sigma_\ell^T$ ,  $\sigma_\ell^E$ ,  $\rho_\ell$  are being replaced with  $D_\ell^{TE}(o)$ ,  $\sigma_\ell^T(o)$ ,  $\sigma_\ell^E(o)$ ,  $\rho_\ell(o)$ , respectively.

## 2. Numerical values of the noise power spectra

The symbolic, so far, noises  $N_\ell^{XX}$  have specific numerical values in concrete experiments. We use evaluations quoted in the WMAP and Planck literature (we adopt the experimental parameters but not the fundamental physics in these references) and apply them to the  $TE$  estimators in the WMAP5 best-fit model (33), (34).

The evaluation of the 5-year WMAP noises, which include the instrumental noise, point sources noise and some systematic errors [50], follows from Ref. [41, 45, 46, 47]. Starting with numerical values for  $\Delta D_\ell^{TT}$ ,  $\Delta D_\ell^{TE}$  cited in [41], and using Eq.(10) from [45] and Eq.(1) from [47], we derive the noise terms  $N_\ell^{TT}$ ,  $N_\ell^{EE}$  and plot them in Fig. 6. We use these graphs when we refer to the WMAP5 noises. The noise power spectra have a weak multipole dependence. For example, when  $\ell = 10$ , one has  $N_\ell^{TT} = 1.46 \times 10^{-2} \mu\text{K}^2$ ,  $N_\ell^{EE} = 2.42 \times 10^{-2} \mu\text{K}^2$ ; while for  $\ell = 100$ , one has  $N_\ell^{TT} = 1.36 \times 10^{-2} \mu\text{K}^2$ ,  $N_\ell^{EE} = 2.59 \times 10^{-2} \mu\text{K}^2$ . (Actually, it seems to us that these numbers somewhat overestimate the true WMAP5 noises, as will be discussed in Sec. VII.)

For the Planck experiment, we use the expected instrumental noise in the 143GHz frequency channel. This channel is supposed to have low foreground levels and the smallest noise. The quoted noise power spectra have no  $\ell$ -dependence [44]:

$$N_\ell^{TT} = 1.53 \times 10^{-4} \mu\text{K}^2, \quad N_\ell^{EE} = N_\ell^{BB} = 5.58 \times 10^{-4} \mu\text{K}^2. \quad (42)$$

It is demonstrated in Eq. (38) that noises degrade the correlation coefficient  $\rho_\ell(o)$ . In the left panel of Fig. 7 we plot  $\rho_\ell(o)$  as a function of  $\ell$  for WMAP5 and Planck experiments in comparison with the no-noise graph from Fig. 1. In the right panel of Fig. 7 we show  $P(D_\ell^{TE}(o) < 0)$  for WMAP5 and Planck experiments in comparison with the

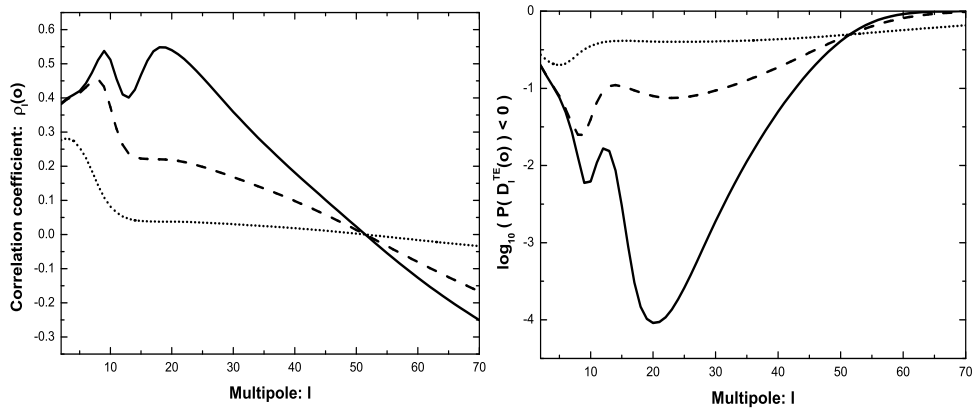


FIG. 7: The correlation coefficient  $\rho_\ell(o)$  (left panel) and the probability  $\log_{10}(D_\ell^{TE}(o) < 0)$  (right panel) in the WMAP5 best-fit model. In both panels the solid, dashed and dotted lines mark the no-noise, Planck and WMAP5 curves, respectively.

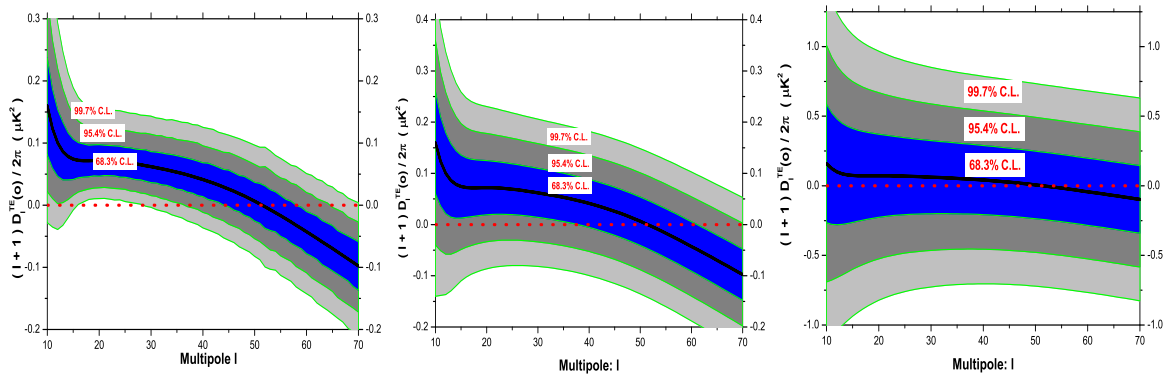


FIG. 8: The 68.3%, 95.4% and 99.7% confidence intervals in the WMAP5 best-fit model. Panels from left to right: no-noise, Planck, WMAP5. Note changes in scaling on the vertical axis.

no-noise graph from Fig. 5. Clearly, large WMAP5 noises make the probability  $P(D_\ell^{TE}(o) < 0)$  dangerously close to 0.5.

In Fig. 8, we show the 68.3%, 95.4%, 99.7% confidence intervals of the  $D_\ell^{TE}(o)$  estimator for Planck and WMAP5 experiments, starting from the no-noise case in the left panel (the same as the left panel in Fig. 4). Obviously, with increasing noise the confidence intervals become progressively wider.

## B. The effects of the cut sky

Some additional stretching of confidence intervals should be attributed to the incomplete sky coverage. Although the shape of the sky cut is, in principle, important for accurate calculations [49], we adopt a simplified approach wherein the available number of degrees of freedom is reduced to  $n = (2\ell + 1)f_{\text{sky}}$ , where  $f_{\text{sky}}$  is the observed portion of the sky. We use the extra symbol  $c$  to denote pdf's in this cut sky approximation. Referring to Eqs. (31), (41) we write

$$f_c(D_\ell^{XX'}(o)) = f(D_\ell^{XX'}(o)) \Big|_{n=(2\ell+1)f_{\text{sky}}}. \quad (43)$$

The mean value of the  $XX'$  estimator calculated with  $f_c(D_\ell^{XX'}(o))$  is the same as in the case of the full sky coverage, but the standard deviation increases,

$$\begin{aligned} \langle D_\ell^{XX}(o) \rangle &= C_\ell^{XX}, \quad \langle D_\ell^{TE}(o) \rangle = C_\ell^{TE}; \\ \Delta D_\ell^{XX}(o) &= \sqrt{\frac{2}{(2\ell+1)f_{\text{sky}}}}(\sigma_\ell^X(o))^2, \quad \Delta D_\ell^{TE}(o) = \sqrt{\frac{(\rho_\ell(o))^2+1}{(2\ell+1)f_{\text{sky}}}}\sigma_\ell^T(o)\sigma_\ell^E(o). \end{aligned} \quad (44)$$

Comparing Eq. (44) with Eqs. (39, 40) we see that the standard deviation increases by the further factor  $1/\sqrt{f_{\text{sky}}}$ . In particular, the confidence intervals in Fig. 8 should be stretched in the vertical direction by this factor.

The WMAP Collaboration [52] and the ‘Planck Blue Book’ [44] quote the cut sky factor

$$f_{\text{sky}}(\text{WMAP}) = 0.85, \quad f_{\text{sky}}(\text{Planck}) = 0.65, \quad (45)$$

respectively. The former one leads to the  $1/\sqrt{f_{\text{sky}}} \approx 1.08$  increase in the uncertainty of the estimators, and the latter one leads to  $1/\sqrt{f_{\text{sky}}} \approx 1.24$ .

In our further analysis we use these stretched confidence intervals, but it may turn out that the quoted noises and  $f_{\text{sky}}$  are overly pessimistic, especially for Planck, so the real level of uncertainty may prove to be smaller.

## VII. TESTS OF THE NULL HYPOTHESIS: WMAP5 BEST-FIT MODEL WITH NO GRAVITATIONAL WAVES

The developed theory can now be confronted with real and simulated data. In Fig. 9, based on information from Ref. [4, 41], we show the WMAP5 unbinned  $TE$  data points on the background of the derived in Sec. VI  $TE$  confidence intervals. Despite the messiness of the picture, the visual impression is such that the curve of the ‘center of gravity’ of the data points lies somewhat below the black solid curve expected of density perturbations alone. This tendency is of course required by the presence of gravitational waves, as we discussed in Sec. V. The visual impression should be quantified by means of the ‘null hypothesis testing’. The null hypothesis under investigation, denoted  $H_0$ , is the WMAP5 best-fit model (33), (34) with no gravitational waves. We probe  $H_0$  with the mean value (M) and the variance (K) tests.

### A. The mean value test

We introduce the statistic  $M$

$$M \equiv \sum_{\ell} \frac{D_\ell^{TE}(o) - C_\ell^{TE}}{\Delta D_\ell^{TE}(o)}. \quad (46)$$

To test observations, one takes  $D_\ell^{TE}(o)$  as the actually observed values of the estimator. The expectation amount  $C_\ell^{TE}$  and the standard deviation  $\Delta D_\ell^{TE}(o)$ , which weighs the scatter of the data points in Eq. (46), are calculated, Eq. (44), according to the hypothesis  $H_0$ . The negative (positive) value of  $M$  quantifies the propensity of the data points to lie below (above) the theoretical prediction. For unbinned data, the summation in Eq. (46) is over  $\ell = 2, 3, \dots, 100$ .

In confirmation of the visual impression, the value of  $M$  on the actually observed  $TE$  data points turns out to be negative and equal to

$$m = -8.69. \quad (47)$$

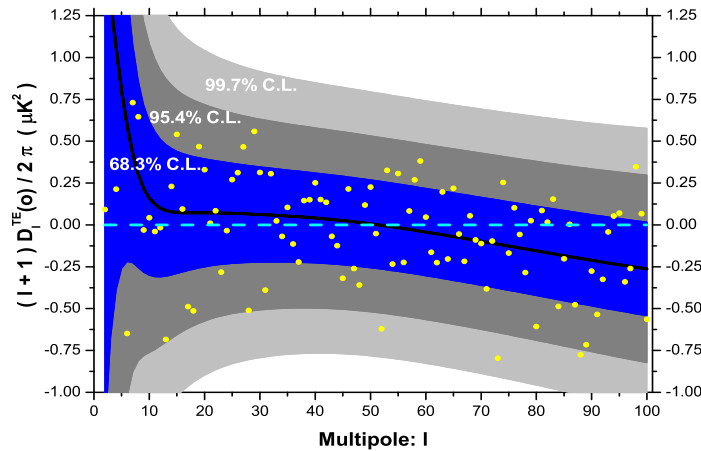


FIG. 9: The WMAP5 unbinned  $TE$  data points on the background of confidence intervals which include WMAP noises from Fig. 6 and  $f_{\text{sky}} = 0.85$ . The black solid line is the expectation value according to the  $H_0$  hypothesis.

To assess the case for rejection of  $H_0$  one needs to know the pdf for the variable  $M$ . Using pdf (43) we generate  $10^4$  random samples of the estimator  $D_\ell^{TE}(o)$ , where each sample includes all  $\ell = 2, 3, \dots, 100$ . We then calculate  $M$  for each sample. The distribution of these  $M$  (effectively, the pdf for the variable  $M$ ) is shown in Fig. 10.

The significance level  $\alpha$  of the test, or in other words the probability of incorrect rejection of  $H_0$ , is

$$\alpha = P \left( |M| \geq |m| \mid H_0 \right).$$

Calculating  $\alpha$  from the pdf in Fig. 10, and with  $m$  from Eq. (47), we find  $\alpha = 40.63\%$ .

$$\alpha = 40.63\%. \quad (48)$$

Although the case for rejection of the hypothesis  $H_0$  is weak, within  $1\sigma$ , Eqs. (47, 48) serve as an indication that one may try to find a better hypothesis.

To check the stability of this conclusion, we expanded the  $M$  test. First, we carried out the same procedure with the 3-year WMAP data and found similar results. Second, we assumed the full sky coverage  $f_{\text{sky}} = 1.0$  with WMAP5 unbinned data and arrived at a slightly stronger evidence for rejection of  $H_0$ ,  $m = -9.43$ ,  $\alpha = 32.91\%$ . Third, we applied the  $M$  test to the WMAP5 data binned at thirteen multipoles  $\ell = 4, 10, 17, 22, 27, 33, 40, 48, 56, 65, 76, 87, 98$  [4, 41], as shown in Fig. 11. We made simplifying theoretical assumptions [53, 54, 55] according to which the estimator at every binned multipole obeys a Gaussian distribution with the mean value  $C_\ell^{TE}$  taken at  $\ell$  representing the bin, and with the standard deviation properly averaged over the bin and reduced by the size of the bin. Binned multipoles are supposed to be statistically independent. In Fig. 11, the binned WMAP5  $TE$  data  $(\ell + 1)D_\ell^{TE}(o)/2\pi$  are shown by blue dots, and the  $1\sigma$  intervals, which include WMAP5 noises from Fig. 6 and  $f_{\text{sky}} = 0.85$ , are shown by blue bars. Following a somewhat incorrect practice, we transferred the  $1\sigma$  confidence intervals from the theoretical pdf to the data points themselves. The size of the bins is indicated by the width of the yellow regions. The black solid line is the expectation value according to  $H_0$  hypothesis. Under the simplifying assumptions made, the quantity  $M$  satisfies a zero-mean Gaussian distribution with variance  $n = 13$ , determined by the number  $n = 13$  of the observed (binned) data points. The analogue of Eq. (46), with summation over thirteen binned multipoles, resulted in  $m = -3.72$ ,  $\alpha = 30.21\%$ . The additional assumption  $f_{\text{sky}} = 1$  reduces  $\alpha$  to  $\alpha = 26.52\%$ .

The crucial importance of efforts to reduce noises in future experiments is illustrated by the following exercise. We assumed that the Planck mission would observe exactly the same  $TE$  data points as WMAP5 did, but which should now be analyzed against the Planck's smaller noises. We first calculated the confidence intervals of the unbinned data using the Planck noises (42) and  $f_{\text{sky}} = 0.65$ , and then we have binned the data using the same procedure that was used in the WMAP analysis [4, 41]. The resulting  $1\sigma$  intervals are shown by red bars in Fig. 11. With these smaller

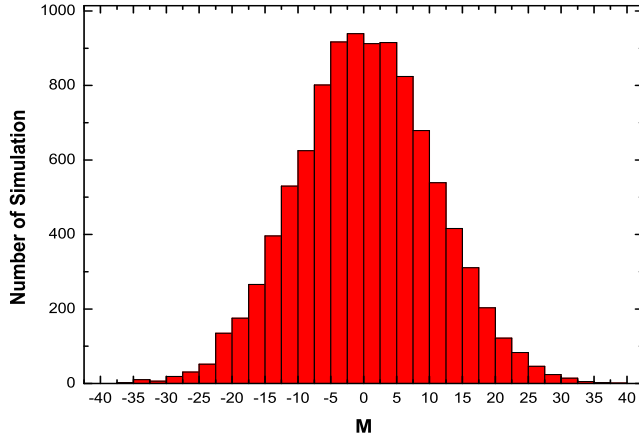


FIG. 10: The outcome values of the test quantity  $M$  in simulated samples. In the actually observed realization,  $m = -8.69$ .

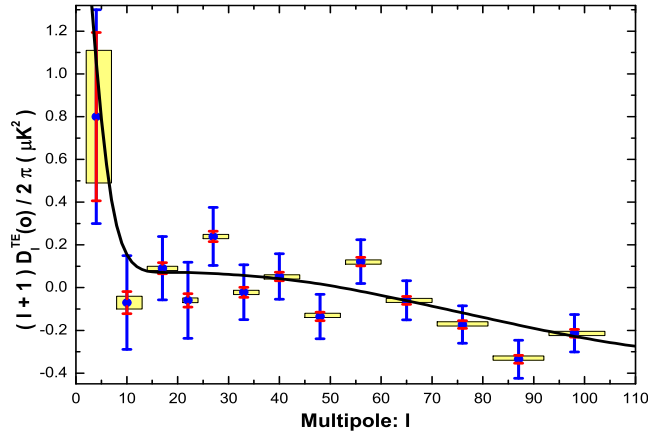


FIG. 11: In this figure, based on 5-year WMAP observations [4, 41], we show binned  $TE$  data points  $(\ell + 1)D_{\ell}^{TE}(o)/2\pi$  surrounded by various  $1\sigma$  uncertainties: WMAP5 (blue, largest), Planck (red, intermediate), no-noise (yellow, smallest).

uncertainties, the  $M$  test gives  $m = -15.67, \alpha = 1.39 \times 10^{-5}$ . The further assumption  $f_{\text{sky}} = 1$  makes  $\alpha$  even smaller,  $\alpha = 7.08 \times 10^{-8}$ . In other words, in these circumstances, the null hypothesis would be rejected at a higher than  $4\sigma$  level ( $\alpha \simeq 7 \times 10^{-5}$ ).

Finally, we have looked at what would happen in the ideal, no-noise, case, that is, when the standard deviation is at its minimum level  $\Delta D_{\ell}^{TE}$  and  $f_{\text{sky}} = 1$ . The  $1\sigma$  intervals are shown by the height of yellow regions in Fig. 11. The  $M$  test results in  $m = -27.17, \alpha = 5.19 \times 10^{-14}$ . Thus, in the ideal case, the WMAP5  $TE$  observations would have rejected the WMAP5  $H_0$  hypothesis at a higher than  $7\sigma$  level. The results of all  $M$  tests are summarized in Table I.

TABLE I: Significance level  $\alpha$  in the mean value tests based on WMAP5 data.

data	noises	$\alpha$ (cut sky)	$\alpha$ (full sky)
unbinned data	WMAP5 noises	40.63%	32.91%
binned data	WMAP5 noises	30.21%	26.52%
binned data	Planck noises	$1.39 \times 10^{-5}$	$7.08 \times 10^{-8}$
binned data	no noise	—	$5.19 \times 10^{-14}$

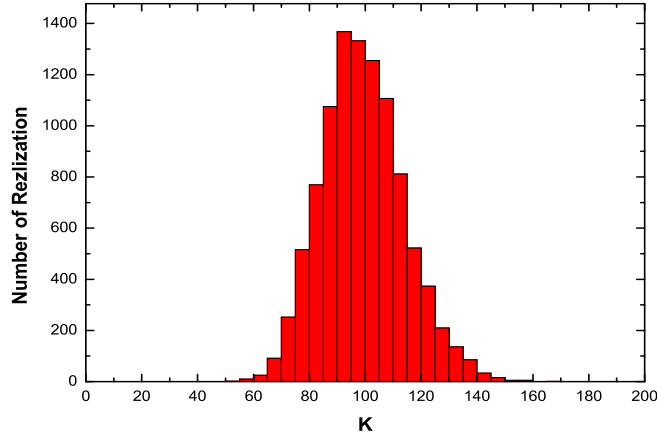


FIG. 12: The distribution of the test quantity  $K$  from the simulated samples. In the observed realization,  $k = 85.38$ .

### B. The variance test

The scatter of the observed data points is probed by the  $K$  statistic

$$K \equiv \sum_{\ell} \frac{(D_{\ell}^{TE}(o) - C_{\ell}^{TE})^2}{(\Delta D_{\ell}^{TE}(o))^2}.$$

The significance level  $\alpha$  of the  $K$  test is defined by

$$\alpha = P\left(K \geq k \mid H_0\right).$$

First, we apply the  $K$  test to the WMAP5  $TE$  unbinned data, shown on Fig. 9. The pdf of the test statistic  $K$ , built by the simulation method described in the previous subsection, is shown in Fig. 12. The value of the  $K$  statistic and the corresponding significance level are as follows  $k = 85.38, \alpha = 82.63\%$ . Under the assumption  $f_{\text{sky}} = 1$ ,  $\alpha$  reduces to  $\alpha = 44.38\%$ . Thus, with WMAP5 noises, the variance test does not provide enough evidence for rejection of the null hypothesis. Nevertheless, the somewhat lower than expected value of  $k$  points toward a possible overestimation of the WMAP5 noises.

We have also applied the  $K$  test to the binned 5-year WMAP data. We have made the same simplifying Gaussian assumptions that were discussed in Sec. VII A. Under these assumptions, the quantity  $K$  obeys a  $\chi_n^2$  distribution with  $n = 13$  degrees of freedom [56]. The peak of this function is at  $K \approx n$ . Using this pdf, we find  $k = 11.48$  and  $\alpha = 57.06\%$ . The full sky assumption reduces  $\alpha$  to  $\alpha = 40.96\%$ . Again, with WMAP5 noises, the case for rejection of  $H_0$  is weak.

The value of  $\alpha$  dramatically decreases when the WMAP5 data are accompanied by the Planck noises. In this case,  $k \approx 211$  and  $\alpha \approx 10^{-37}$ . The  $H_0$  hypothesis would have been rejected with a huge margin. The  $\alpha$  is even smaller in the no-noise case with  $f_{\text{sky}} = 1$ . The summary of  $K$  tests is shown in Table II.

TABLE II: The significance level  $\alpha$  of  $K$  tests of WMAP5 data

data	noises	$\alpha$ (cut sky)	$\alpha$ (full sky)
unbinned data	WMAP noises	82.63%	44.38%
binned data	WMAP noises	57.06%	40.96%
binned data	Planck noises	$\approx 10^{-37}$	$< 10^{-37}$
binned data	no noise	—	$\ll 10^{-37}$

It is important to note that, with the Gaussian approximations made for the pdf of the estimator  $D_\ell^{TE}(o)$ , the variance test is equivalent to the test, where the calculations are being done directly with the weighted values of the pdf at individual data points:

$$K = -2 \ln \left( \frac{\prod_\ell f(D_\ell^{TE}(o))}{\prod_\ell f(C_\ell^{TE})} \right) = -2 \ln \prod_\ell \frac{f(D_\ell^{TE}(o))}{f(C_\ell^{TE})}, \quad (49)$$

where  $f(D_\ell^{TE}(o))$  is the value of the pdf at the observed data point  $D_\ell^{TE}(o)$ , and  $f(C_\ell^{TE})$  is the value of the pdf at the expected point  $D_\ell^{TE}(o) = C_\ell^{TE}$ .

## VIII. LIKELIHOOD ANALYSIS OF THE QUADRUPOLE RATIO $R$

The existence of relic gravitational waves is a necessity dictated by general relativity and quantum mechanics, and not an inflationary ‘bonus’ which, as follows from inflationary theory, most likely should not be awarded, see Sec. II. We do not use our theoretical position as a technical ‘prior’ in data analysis, but we certainly are willing to reconsider the WMAP5  $TE$  data from this point of view. We also intend to make predictions for future experiments. The immediate goal is to evaluate the quadrupole parameter  $R$ , Eq. (36), from the existing observations. The mild indications in the WMAP5  $TE$  data favoring the rejection of the  $H_0$  hypothesis ( $R = 0$ ) have been discussed above.

### A. Expanding the parameter space

The inclusion of gravitational waves with two new free parameters  $B_t^2$  and  $n_t$  (see Eq. (4)) would require, strictly speaking, a new full-scale likelihood analysis of all the data. Certainly, the addition of gravitational waves must be consistent with all the measured correlation functions and upper limits, Eq. (15). In what follows, we simplify this approach, while retaining the main points of what we want to demonstrate. First, we keep intact the background cosmological parameters, as quoted in Eq. (33). Second, we bound the four perturbation parameters  $B_s^2$ ,  $n_s$ ,  $B_t^2$ ,  $n_t$  by three constraints, thus leaving independent only one parameter. We choose this independent parameter to be the quadrupole ratio  $R$ . The three mentioned constraints are as follows:

$$n_t = n_s - 1, \quad \ell(\ell + 1)C_{\ell=10}^{TT}/2\pi = 840\mu\text{K}^2, \quad n_s(R) = n_s(0) + 0.35R - 0.07R^2. \quad (50)$$

The first constraint is purely theoretical, it reflects the origin of cosmological perturbations [40]. The second constraint plays the role of an overall normalization, it requires the perturbation parameters to satisfy the demand that the joint,  $dp$  plus  $gw$ , temperature anisotropy at  $\ell = 10$  were fixed at the well-measured level. The third constraint, where  $n_s(0) = 0.960$  [4], is empirical. The function  $n_s(R)$  was designed to be such that the best studied correlation function  $C_\ell^{TT}$  were as close as possible to the actually observed data for a wide range of possible  $R \geq 0$ . In contrast to other analyses, we are not using the inflationary ‘consistency relation’  $n_t = -r/8$ , which affects the results regarding gravitational waves (see comments in [2] on the self-contradictory nature of the data analysis based on inflationary formulas).

In Fig. 13 we illustrate, for selected values of  $R$ , the consistency of our class of models with the  $TT$  and  $EE$  observations. As usual, some corrections at very high  $\ell$ 's could be achieved, if desired, by the assumption of the ‘running’ spectral index  $n_s$ , but we did not resort to this possibility. It is also important to emphasize that the  $BB$  spectrum in our class of models is well below the existing upper limits [47]. Indeed, the WMAP limit is  $\ell(\ell + 1)C_{\ell=2-6}^{BB}/2\pi < 0.15\mu\text{K}^2$  (95% C.L.). This corresponds to  $r < 20$  [47], which is roughly  $R < 10$ , whereas we will be mostly dealing with  $R < 1$ .



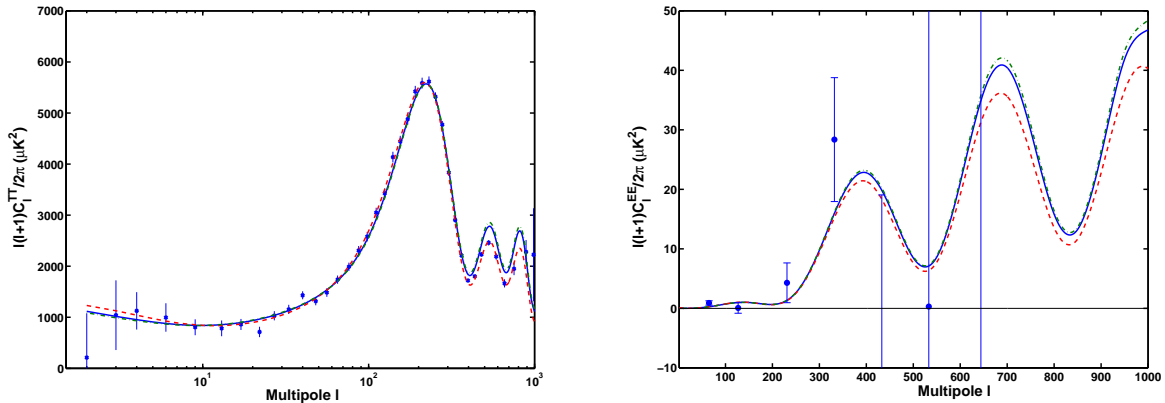


FIG. 13: The  $TT$  (left) and  $EE$  (right) power spectra in models with varying amounts of gravitational waves. The dashed (red) line is for the  $H_0$  hypothesis,  $R = 0$ . The solid (blue) line shows the model with  $R = 0.24$ , and the dash-dotted (green) line is for the model with  $R = 0.3$ .

### B. Likelihood function for $R$ from the WMAP $TE$ data

The likelihood function for a parameter is a pdf for a random variable, where the parameter is considered unknown, whereas the value of the random variable is considered known from experiment (see for example [29, 49, 57]). Since the variables  $D_\ell^{TE}(o)$  with differing  $\ell$ 's are independent, their joint pdf is a product of individual pdf's  $f_c(D_\ell^{TE}(o))$  over  $\ell$ . Therefore, the likelihood function for  $R$  is

$$\mathcal{L}(R) = C \prod_{\ell} f_c(D_\ell^{TE}(o)), \quad (51)$$

where  $f_c(D_\ell^{TE}(o))$  is given by Eqs. (43, 41), the quantities  $D_\ell^{TE}(o)$  are taken from observations, and  $C$  is a normalization constant to be fixed later.

Moving by small steps  $\Delta R = 0.01$  from  $R = 0$  we build  $\mathcal{L}(R)$  numerically. The  $D_\ell^{TE}(o)$  participating in Eq. (51) are the unbinned data shown in Fig. 9, the other quantities are determined by Eqs. (33, 50), Fig. 6 and  $f_{\text{sky}} = 0.85$ . The result of this calculation is shown by a solid line in Fig. 14.

The maximum of  $\mathcal{L}(R)$  is at  $R = 0.240$ . The constant  $C$  was chosen to make  $\mathcal{L}(R) = 1$  at maximum, as illustrated in Fig. 14. Taking into account  $R = 0.240$  and Eq. (50), the full set of our best-fit perturbation parameters is defined by

$$\ell(\ell + 1)C_{\ell=10}^{TT}/2\pi = 840\mu\text{K}^2, \quad R = 0.240, \quad n_s = 1.040, \quad n_t = 0.040. \quad (52)$$

This model has a blue(ish) primordial power spectrum and accommodates a significant amount of relic gravitational waves. The  $TE$  spectrum for this model is shown by a solid line in Fig. 15. The main difference with the  $TE$  spectrum of the WMAP5 best-fit model (dashed line) is at multipoles  $\ell < 50$ . This could be anticipated, as the role of gravitational waves is essential only at  $\ell \lesssim 100$ . The  $TT$  and  $EE$  spectra for our model ( $R = 0.240$ ) are plotted in Fig. 13.

The difference with WMAP conclusions is indicative but not significant, owing to large WMAP noises. Indeed, the confidence interval around the maximum likelihood value  $R = 0.240$  is broad. Using the techniques of Appendix A we find that the 68.3% confidence interval is represented by  $R = 0.240_{-0.225}^{+0.291}$ . (Lower boundary cannot be less than  $-0.240$  as the quantity  $R$  is non-negative.) Thus, the value  $R = 0$  is only barely outside the 68.3% confidence interval. This result is consistent with the null hypothesis testing in Sec. VII.

We have also calculated the likelihood function  $\mathcal{L}(R)$  for 3-year WMAP  $TE$  data. The background cosmological parameters are taken as the WMAP3  $\Lambda$ CDM model:  $\Omega_m h^2 = 0.1265$ ,  $\Omega_b h^2 = 0.0223$ ,  $h = 0.735$ ,  $\tau_{\text{reion}} = 0.088$  [58]. In line with the WMAP3 findings we set  $n_s(0) = 0.951$  [58] and use Eq. (50) to relate  $n_s$  and  $R$ . The resulting likelihood function is shown in Fig. 14 by a dashed line. The maximum likelihood value, along with the associated 68% confidence interval, is  $R = 0.149_{-0.149}^{+0.247}$ . The best-fit spectral indices are  $n_s = 1.002$  and  $n_t = 0.002$ . Again, the  $R = 0$  is within the 68.3% confidence interval. Nevertheless, it is worth noting that in transition from WMAP3 to WMAP5 data, the peak value of  $R$  increased from  $R = 0.149$  to  $R = 0.240$ .

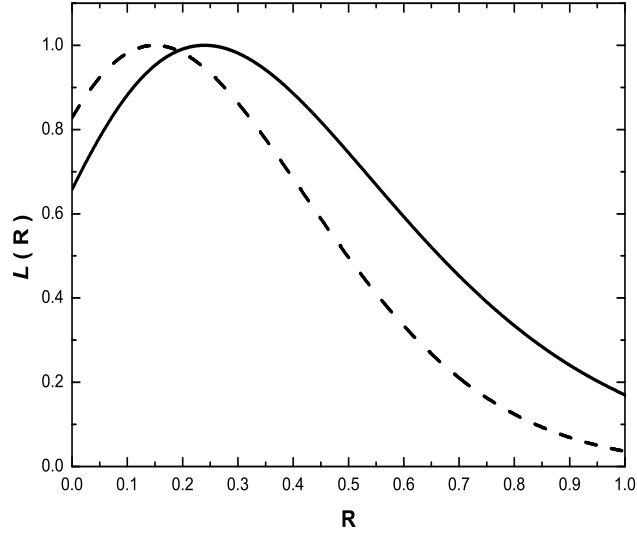


FIG. 14: The likelihood function for  $R$ . The solid line uses the unbinned 5-year WMAP data, whereas the dashed line is for the unbinned 3-year WMAP data.

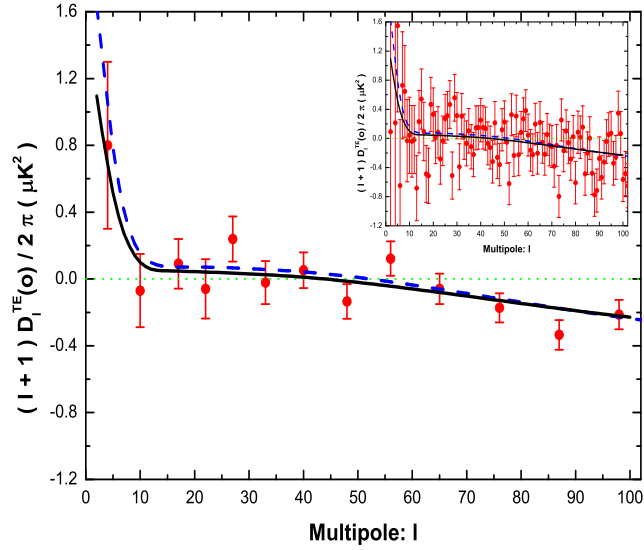


FIG. 15: The solid line is our best fit to the WMAP5 binned  $TE$  data, in comparison with the  $H_0$  hypothesis (dashed line). The depicted error bars are taken from the  $R = 0$  model. In the insert, we plot the same graph for unbinned data.

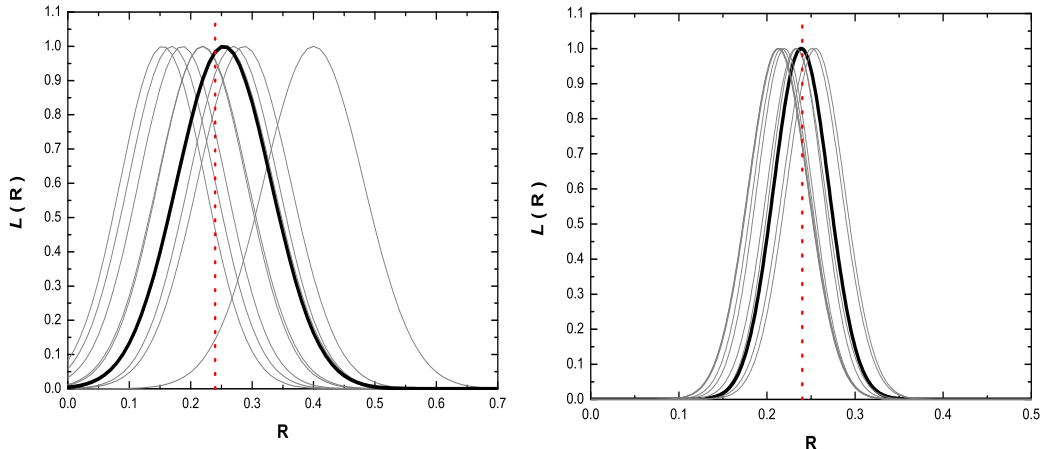


FIG. 16: The likelihood functions for  $R$  with the input value  $R_i = 0.240$ . The Planck conditions are used in the left panel, the ideal conditions - in the right panel. The ‘typical’ likelihood functions are shown by the dark lines.

### C. Likelihood analysis of simulated $TE$ data

Being guided by the experience that in astrophysics very often ‘today’s indication is tomorrow’s discovery’, we treat our best-fit model (52) as a benchmark model to be confirmed by Planck and other sensitive missions. Using the parameters of this model we simulate the  $TE$  data for Planck, taking into account the expected noises and  $f_{\text{sky}}$ . We also vary the perturbation parameters, noises and sky coverage in order to assess what will be happening with nearby models.

The procedure for Planck is as follows. First, we choose the input value  $R_i$  and determine other perturbation parameters from Eq. (50). The background parameters are fixed by Eq. (33). Second, we adopt Planck parameters, Eqs. (42, 45), and randomly generate 10 sets of data points  $\{D_\ell^{TE}(o) | \ell = 2, 3, \dots, 100\}$ , where each set includes all indicated  $\ell$ ’s. We use for this purpose the underlying pdf  $f_c(D_\ell^{TE}(o))$ , Eqs. (43, 41). Obviously, even if all parameters are fixed, the outcome data points  $D_\ell^{TE}(o)$  are supposed to be random due to the randomness of signal and noises. Third, for every set of simulated data we build, in a manner described in Sec. VIII B, the likelihood functions  $\mathcal{L}(R)$  and explore their properties.

Let us start from the benchmark value  $R_i = 0.24$ . The 10 likelihood functions built from 10 random realizations are shown in Fig. 16 (left plot). As expected, the maxima of the likelihood functions concentrate around the input value  $R_i = 0.240$ , and the widths of the likelihood functions are approximately equal to each other. The arithmetical mean of the maxima is  $\overline{R_p} = 0.242$ , and the arithmetical mean width of the 68.3% confidence intervals, i.e.  $1\sigma$  interval, is  $\overline{\Delta R} = 0.074$ . The realization whose maximum is closest to the input value  $R_i = 0.240$  (in a sense, a ‘typical’ likelihood function) is shown by a dark line.

On the ground of these simulations we conclude that the Planck satellite will be able to see a relatively strong evidence for relic gravitational waves, if the  $R_i = 0.240$  model is correct. In other words, Planck will be able to exclude the value  $R = 0$  at more than  $3\sigma$  confidence level. We have also done simulations for a more optimistic cut sky factor  $f_{\text{sky}} = 0.85$ . In this case,  $\overline{\Delta R} = 0.062$ , thus allowing to exclude the  $R = 0$  assumption at  $4\sigma$  level.

The best achievable conditions for detecting the signature of relic gravitational waves are reached in the idealized case of no noise and full sky coverage. With the input value  $R_i = 0.240$ , the 10 likelihood functions for  $TE$  experiment in ideal conditions are shown in Fig. 16 (right plot). The mean value of the maxima is  $\overline{R_p} = 0.228$ , and the mean width of the 68.3% confidence intervals is  $\overline{\Delta R} = 0.032$ . Thus, the ideal  $TE$  experiment would be able to detect gravitational waves and exclude  $R = 0$  at more than  $7\sigma$  confidence level.

We have also evaluated the  $R$  detectable at a  $2\sigma$  level by Planck or ideal experiment. In the left panel of Fig. 17

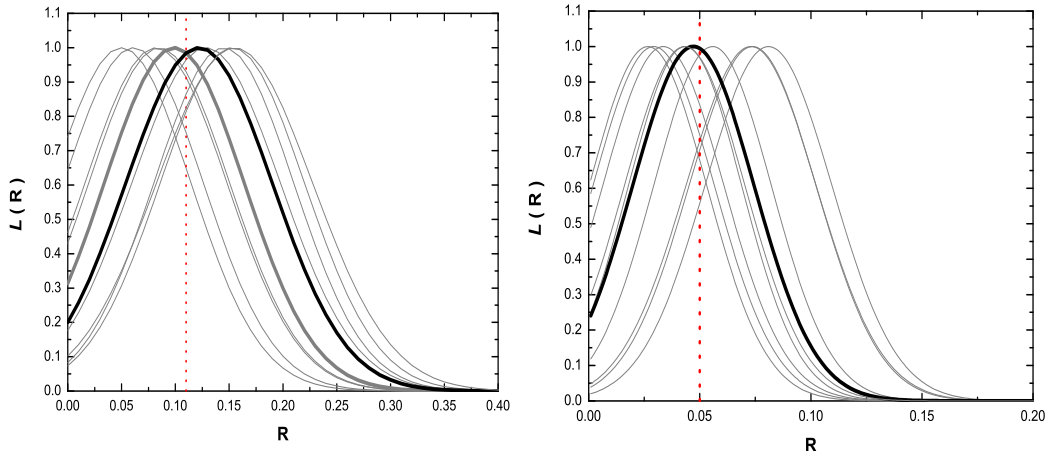


FIG. 17: The likelihood functions for the smallest  $R$  detectable at a  $2\sigma$  level. The left panel uses  $R_i = 0.110$  and Planck parameters. The right panel is for an ideal experiment with  $R_i = 0.050$ . The ‘typical’ functions are shown by dark lines.

we show 10 likelihood functions for the input  $R_i = 0.110$  and Planck parameters. The mean value of the maxima is at  $\overline{R}_p = 0.108$ , and the mean width of the  $1\sigma$  confidence intervals is  $\overline{\Delta R} = 0.067$ . Thus, using the  $TE$  method, the Planck satellite would be able to detect  $R = 0.110$  at nearly  $2\sigma$  level. The left panel of Fig. 17 shows the results of solving the same problem in the ideal case. The input  $R$  for the 10 likelihoods is  $R_i = 0.050$ . The mean value of the peaks is  $\overline{R}_p = 0.051$ , and the mean width of the  $1\sigma$  confidence intervals is  $\overline{\Delta R} = 0.025$ . Thus, an ideal experiment would detect  $R = 0.05$  at exactly  $2\sigma$  level. Even more possibilities are considered below in the context of comparison of  $TE$  and  $BB$  methods.

## IX. COMPARISON OF $TE$ AND $BB$ METHODS IN SEARCH FOR RELIC GRAVITATIONAL WAVES AND PROSPECTS FOR THE PLANCK MISSION

The advantage of the usually discussed  $B$ -mode searches for primordial gravitational waves is that in the  $BB$  correlation function there is no competing contribution from density perturbations. However, the  $BB$  signal is inherently weak, it is about 50 times smaller than the  $g.w.$  contribution to the  $TE$  correlation. It is true that the nominal  $BB$  noise is also smaller than the  $TE$  noise, so that the nominal ‘signal to noise’ ratio may be slightly in favor of the  $BB$  method. But one must take into account the large systematic effects that the  $B$ -mode is prone to. They include the various contaminations [32, 59, 60, 61], the disadvantages of dealing with an auto-correlation ( $BB$ ) rather than with a cross-correlation ( $TE$ ) function, the actual weakness of the signal which can lead to the danger of unexpected leakages and couplings, etc. It is only the experimenters who can properly assess these complications.

When only the evaluation of the Planck’s instrumental  $BB$  noise, Eq. (42), is used in calculations, we call it an ‘optimistic’  $BB$  case. As for the additional complications mentioned above, we try to treat them as ‘effective’ noises in the framework of our formalism. We give our evaluation of these ‘effective’ noises and increase the nominal instrumental  $BB$  noise to the level which we call the ‘realistic’  $BB$  case. We think that it is only this ‘realistic’  $BB$  case that can be taken as a fair comparison with the  $TE$  method. The comparison of  $TE$  and  $BB$  methods was also considered in a recent paper [34] (see also earlier papers [62, 63]).

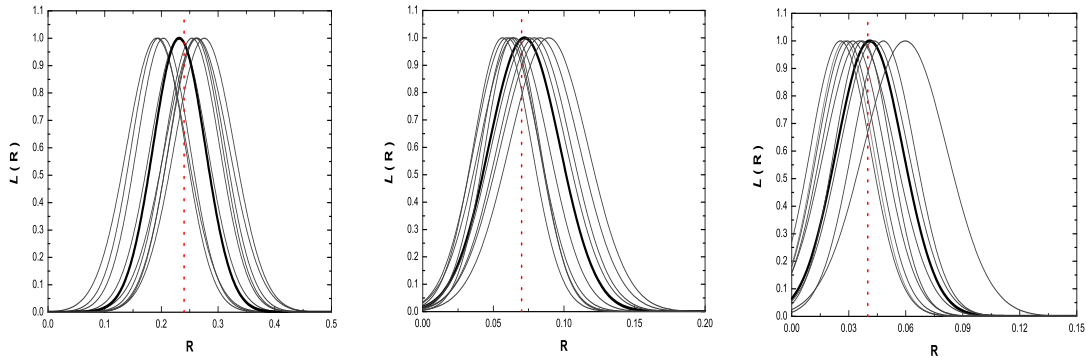


FIG. 18: Likelihood functions for  $R$  from simulated  $BB$  data with Planck parameters  $N_\ell^{BB} = 5.58 \times 10^{-4} \mu\text{K}^2$ ,  $f_{\text{sky}} = 0.65$ . The input values in the panels from left to right are  $R_i = 0.24, 0.07, 0.04$ . The dark solid lines show the ‘typical’ likelihood functions.

### A. The likelihood function for $R$ in the $BB$ method

We start from the ‘optimistic’  $BB$  case where the  $BB$  noise is taken as  $N_\ell^{BB} = 5.58 \times 10^{-4} \mu\text{K}^2$ , see Eq. (42). We generate the mock  $BB$  data using the pdf  $f_c(D_\ell^{BB}(o))$  from Eq. (43), Eq. (24) (setting  $XX = BB$ ), and Eq. (45). The procedure is exactly the same as was described in Sec. VIII C in the context of the  $TE$  mock data. The 10 sets of simulated data for every input  $R_i$  are then used in the likelihood function

$$\mathcal{L}(R) = C \prod_{\ell} f_c(D_\ell^{BB}(o)),$$

where  $C$  is a normalization constant.

First, we discuss the benchmark model  $R_i = 0.240$ . The 10 likelihood functions are shown in Fig. 18 (left panel). The mean value of the maxima is  $\overline{R_p} = 0.237$ . The mean width of the 68.3% confidence intervals is  $\overline{\Delta R} = 0.050$ . This is a bit smaller than the mean width in the  $TE$  likelihood functions. For illustration, we considered other examples as well. The 10 likelihood functions with the input value  $R_i = 0.070$  are plotted in the middle panel of Fig. 18. The mean values are  $\overline{R_p} = 0.070$  and  $\overline{\Delta R} = 0.024$ . This shows that  $R = 0.070$  could be detected by the  $BB$  method at nearly  $3\sigma$  level. Finally, the likelihood functions with the input value  $R_i = 0.040$  are shown in the right plot of Fig. 18. The mean values are  $\overline{R_p} = 0.038$ ,  $\overline{\Delta R} = 0.018$ . This  $R$  is at somewhat better than  $2\sigma$  level of detection.

Introducing the quantity

$$\frac{S}{N} \equiv \frac{R_i}{\overline{\Delta R}}$$

as the ‘signal to noise’ measure of detecting gravitational waves, we show in Table III the comparative performances of  $TE$  and ‘optimistic’  $BB$  methods in terms of  $S/N$  for a range of input values  $R_i$ . The Table also shows the mean values  $\overline{R_p}$  of the maxima of the likelihood functions and the mean widths  $\overline{\Delta R}$  of the 68.3% confidence intervals. (The number of displayed decimal digits is an artefact of numerical calculations, and not a demonstration of our responsibility for the accuracy of results.)

Moving to the discussion of the ‘realistic’  $BB$  case, we think that all the non-instrumental ‘effective’ noises can increase the level of the noise variables  $a_{\ell m}^B(n)$ , Sec. VI, by at least a factor of 2. This means that the noise term  $N_\ell^{BB}$  participating in our analysis, should be raised from its level in Eq. (42) by at least a factor of 4. In other words, we are working with the ‘realistic’ noise term  $N_\ell^{BB} = 2.24 \times 10^{-3} \mu\text{K}^2$ . Repeating all the calculations with this noise term, we come up with the ‘realistic’ evaluation of the Planck’s  $BB$  performance, as shown in Table IV.

TABLE III: Comparison of the  $TE$  and ‘optimistic’  $BB$  methods in terms of the signal to noise ratio  $S/N$ .

$R_i$	0.30	0.24	0.20	0.15	0.11	0.07	0.04
TE: $\overline{R_p}$	0.28	0.24	0.19	0.13	0.11	0.07	—
TE: $\overline{\Delta R}$	0.08	0.07	0.07	0.07	0.07	0.07	—
TE: $S/N$	3.90	3.24	2.82	2.21	1.64	1.06	—
BB: $\overline{R_p}$	0.31	0.24	0.20	0.16	0.11	0.07	0.04
BB: $\overline{\Delta R}$	0.06	0.05	0.04	0.04	0.03	0.02	0.02
BB: $S/N$	5.36	4.80	4.55	3.95	3.44	2.92	2.22

TABLE IV: Signal to noise ratio  $S/N$  in the ‘realistic’  $BB$  case.

$R_i$	0.30	0.24	0.20	0.15	0.11	0.07
BB: $\overline{R_p}$	0.29	0.26	0.20	0.15	0.10	0.06
BB: $\overline{\Delta R}$	0.13	0.11	0.09	0.07	0.06	0.05
BB: $S/N$	2.40	2.24	2.30	2.06	1.72	1.32

The numerical results for  $TE$  and  $BB$  methods are also presented as individual  $S/N$  points in Fig. 19. The solid lines in this figure show the analytical approximations which we are set to discuss.

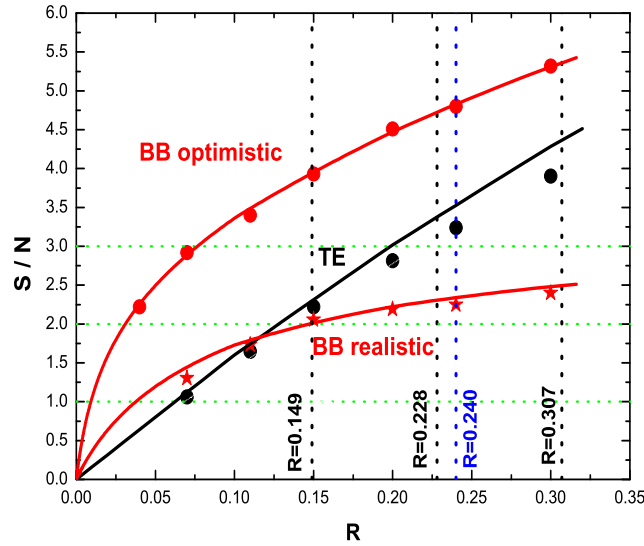


FIG. 19: The signal to noise ratio  $S/N$  as a function of  $R$  for the  $TE$  (black) and  $BB$  (red) methods. The points show numerical results, whereas the curves are analytical approximations.

## B. Understanding the signal to noise ratio $S/N$ in $TE$ and $BB$ methods

Our numerical calculations are supported by simple analytical expressions for  $S/N$  in  $TE$  and  $BB$  methods. Let  $XX'$  denote either  $TE$  or  $BB$ . With Gaussian approximation for individual pdfs, Eq. (37), and given the statistical independence of differing  $\ell$ 's, the likelihood function  $\mathcal{L}(R)$  reads

$$\mathcal{L}(R) = \prod_{\ell=2}^{\ell_{max}} \frac{1}{\sqrt{2\pi}\Delta D_{\ell}^{XX'}} \exp \left[ -\frac{1}{2} \left( \frac{D_{\ell}^{XX'} - C_{\ell}^{XX'}}{\Delta D_{\ell}^{XX'}} \right)^2 \right].$$

The  $R$ -dependence of  $\mathcal{L}(R)$  is coming from the  $R$ -dependence of  $C_{\ell}^{XX'}$  and  $\Delta D_{\ell}^{XX'}$ .

The estimate of the width  $\Delta R$  of  $\mathcal{L}(R)$  with the input (maximum likelihood) value  $R = R_i$  is given by [64]

$$\Delta R = \left[ - \left\langle \frac{\partial^2 \ln \mathcal{L}(R)}{\partial R^2} \Big|_{R=R_i} \right\rangle \right]^{-\frac{1}{2}}, \quad (53)$$

where the angle brackets denote the average over the joint pdf for  $D_{\ell}^{XX'}$ . The second derivative participating in Eq. (53) is

$$\begin{aligned} -\frac{\partial^2 \ln \mathcal{L}(R)}{\partial R^2} &= \sum_{\ell=2}^{\ell_{max}} \frac{1}{\Delta D_{\ell}^{XX'^2}} \left\{ \left( \frac{\partial C_{\ell}^{XX'}}{\partial R} \right)^2 + \left[ - \left( D_{\ell}^{XX'} - C_{\ell}^{XX'} \right) \frac{\partial^2 C_{\ell}^{XX'}}{\partial R^2} \right. \right. \\ &+ \frac{4 \left( D_{\ell}^{XX'} - C_{\ell}^{XX'} \right) \frac{\partial C_{\ell}^{XX'}}{\partial R} \frac{\partial \Delta D_{\ell}^{XX'}}{\partial R}}{\Delta D_{\ell}^{XX'}} \\ &+ \left( \frac{3 \left( D_{\ell}^{XX'} - C_{\ell}^{XX'} \right)^2 - \Delta D_{\ell}^{XX'^2}}{\Delta D_{\ell}^{XX'^2}} \right) \left( \frac{\partial \Delta D_{\ell}^{XX'}}{\partial R} \right)^2 \\ &+ \left\{ - \left( D_{\ell}^{XX'} - C_{\ell}^{XX'} \right) \frac{\partial^2 C_{\ell}^{XX'}}{\partial R^2} + \frac{4 \left( D_{\ell}^{XX'} - C_{\ell}^{XX'} \right) \frac{\partial C_{\ell}^{XX'}}{\partial R} \frac{\partial \Delta D_{\ell}^{XX'}}{\partial R}}{\Delta D_{\ell}^{XX'}} \right. \\ &+ \left( \frac{3 \left( D_{\ell}^{XX'} - C_{\ell}^{XX'} \right)^2 - \Delta D_{\ell}^{XX'^2}}{\Delta D_{\ell}^{XX'^2}} \right) \left( \frac{\partial \Delta D_{\ell}^{XX'}}{\partial R} \right)^2 \\ &\left. \left. + \left( \frac{\Delta D_{\ell}^{XX'^2} - \left( D_{\ell}^{XX'} - C_{\ell}^{XX'} \right)^2}{\Delta D_{\ell}^{XX'}} \right) \left( \frac{\partial^2 \Delta D_{\ell}^{XX'}}{\partial R^2} \right) \right] \right\}. \end{aligned}$$

Using the averages

$$\langle D_{\ell}^{XX'} \rangle = C_{\ell}^{XX'}, \quad \left\langle \left( D_{\ell}^{XX'} - C_{\ell}^{XX'} \right)^2 \right\rangle = \Delta D_{\ell}^{XX'^2}$$

we arrive at an intermediate expression

$$\Delta R = \left[ \sum_{\ell=2}^{\ell_{max}} \frac{1}{\Delta D_{\ell}^{XX'^2}} \left( \left( \frac{\partial C_{\ell}^{XX'}}{\partial R} \right)^2 + 2 \left( \frac{\partial \Delta D_{\ell}^{XX'}}{\partial R} \right)^2 \right) \right]^{-\frac{1}{2}}. \quad (54)$$

Since the noises are  $R$ -independent and  $\partial \Delta D_{\ell}^{XX'}/\partial R$  is smaller than  $\partial C_{\ell}^{XX'}/\partial R$  by a factor  $\propto 1/\sqrt{(2\ell+1)f_{\text{sky}}}$ , one can neglect the second term in Eq. (54) bringing it to

$$\Delta R = \left[ \sum_{\ell=2}^{\ell_{max}} \left( \frac{1}{\Delta D_{\ell}^{XX'}} \frac{\partial C_{\ell}^{XX'}}{\partial R} \right)^2 \right]^{-\frac{1}{2}}. \quad (55)$$

The general expression (55) is a well-known result [64] applied to CMB subjects on several occasions (see for example [65, 66]). Eq. (55) allows one to write the following analytical estimate for  $S/N$ :

$$S/N = \frac{R}{\Delta R} = \sqrt{\sum_{\ell=2}^{\ell_{max}} \left( \frac{1}{\Delta D_{\ell}^{XX'}} \frac{\partial C_{\ell}^{XX'}}{\partial \ln R} \right)^2}. \quad (56)$$

The further simplifications of Eq. (56) rely on further assumptions. It is reasonable to assume that for sufficiently small  $R$  one can use the Taylor expansion

$$C_{\ell}^{XX'}(R) = C_{\ell}^{XX'} \Big|_{R=0} + R \left( \frac{\partial C_{\ell}^{XX'}}{\partial R} \Big|_{R=0} \right). \quad (57)$$

Then, for  $XX' = TE$  one derives

$$S/N = \sqrt{\sum_{\ell=2}^{\ell_{max}} \left( \frac{C_{\ell}^{TE}(R) - C_{\ell}^{TE} \Big|_{R=0}}{\Delta D_{\ell}^{TE}} \right)^2}, \quad (58)$$

and for  $XX' = BB$  one derives

$$S/N = \sqrt{\sum_{\ell=2}^{\ell_{max}} \left( \frac{C_{\ell}^{BB}(R)}{\Delta D_{\ell}^{BB}} \right)^2}. \quad (59)$$

These expressions could be expected on physical grounds. In the  $TE$  case, the quantity  $C_{\ell}^{TE} \Big|_{R=0}$  is not zero, and it is entirely determined by density perturbations. Therefore, it is reasonable that the  $R$ -signal, allowing to detect gravitational waves, is given (at each  $\ell$ ) by the difference  $C_{\ell}^{TE}(R) - C_{\ell}^{TE} \Big|_{R=0}$ , whereas the  $R$ -noise is given by the total standard deviation  $\Delta D_{\ell}^{TE}$ . In the  $BB$  case, the quantity  $C_{\ell}^{BB} \Big|_{R=0}$  is zero (no gravitational waves - no  $BB$  correlation), and therefore it is reasonable that the  $R$ -signal is given by  $C_{\ell}^{BB}(R)$ , whereas the  $R$ -noise is given by  $\Delta D_{\ell}^{BB}$ .

As one could anticipate, the linear approximation (57) is not quite good for not too small  $R$ . Some deviations from exact numerical results could be expected. However, in Fig. 19, we plot the  $TE$  curve without any corrections, that is, as it follows from the analytical formula (58). As for the  $BB$  case, the noticeable deviations exist, so a better fit to the exact numerical results requires a small correction to Eq. (59). The actually plotted  $BB$  curves in Fig. 19 are given by the corrected analytical formula

$$S/N = \sqrt{\sum_{\ell=2}^{\ell_{max}} \left( \frac{1}{(1+0.5R)} \frac{C_{\ell}^{BB}(R)}{\Delta D_{\ell}^{BB}} \right)^2}. \quad (60)$$

The analytical results shown in Fig. 19 are based on  $\ell_{max} = 100$ .

It is natural that the total  $(S/N)^2$  consists of individual contributions  $(S/N)_{\ell}^2$  at each  $\ell$ . Both, Eq. (58) and Eq. (60), have the structure

$$(S/N)^2 = \sum_{\ell=2}^{\ell_{max}} (S/N)_{\ell}^2,$$

where the individual signal to noise ratios  $(S/N)_{\ell}$  are given by

$$(S/N)_{\ell}^{TE} = \frac{C_{\ell}^{TE}(R) - C_{\ell}^{TE}(R=0)}{\Delta D_{\ell}^{TE}}, \quad (S/N)_{\ell}^{BB} = \frac{(1+0.5R)^{-1} C_{\ell}^{BB}(R)}{\Delta D_{\ell}^{BB}}. \quad (61)$$

One can say that the numerators in Eq. (61) are signals depending on  $R$ , while the denominators are noises. Signals and noises are shown, as functions of  $\ell$ , in Fig. 20 for our benchmark model with  $R = 0.24$ . The lower solid black line for the  $BB$  power spectrum includes the correcting factor  $(1+0.5R)^{-1}$ , whereas the upper solid black line does not.

Fig. 20 provides a graphical illustration of what the signal to noise ratio  $S/N$  in Fig. 19 consists of and how it is being accumulated from the individual, predominantly lower than the noise, contributions at each  $\ell$ . It is seen from



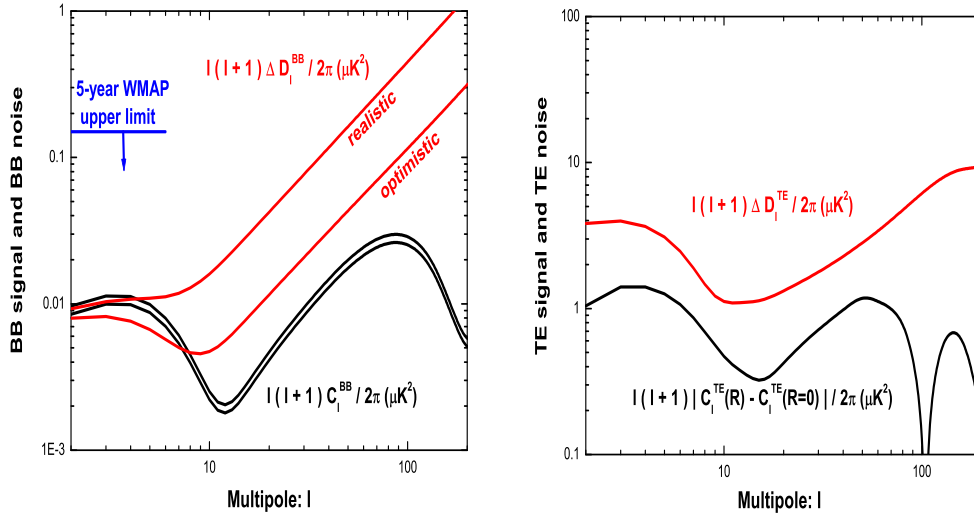


FIG. 20: The  $BB$  and  $TE$  gravitational wave signals (power spectra) in comparison with noises (standard deviations) in the benchmark model  $R = 0.24$ . The signals are in black, the noises are in red.

Fig. 20 that the success of the  $BB$  method strongly relies on the very low multipoles,  $\ell \lesssim 10$ , and hence on the era of reionization with the optical depth  $\tau$  from Eq. (33). Most of  $S/N$  in the  $BB$  method comes from these multipoles [3, 22, 44]. Specifically, in the  $R = 0.24$  model we find

$$\left( \frac{\sum_{\ell=2}^{10} (S/N)_{\ell}^2}{\sum_{\ell=2}^{100} (S/N)_{\ell}^2} \right)_{\text{optimistic}} \simeq 0.47, \quad \left( \frac{\sum_{\ell=2}^{10} (S/N)_{\ell}^2}{\sum_{\ell=2}^{100} (S/N)_{\ell}^2} \right)_{\text{realistic}} \simeq 0.83.$$

The cosmic reionization remains to be fully understood and quantified [67]. If it happens that the optical depth is actually smaller than the currently accepted  $\tau_{reion} \approx 0.08$ , the sensitivity of  $BB$  method to relic gravitational waves will be reduced. On the other hand, if the  $BB$  detection does take place, it will be an argument for the currently accepted or higher  $\tau$ .

In contrast to  $BB$ , the  $TE$  method does not rely on very low multipoles. In fact, the most of  $S/N$  comes from the multipoles  $30 \lesssim \ell \lesssim 70$ . Specifically, in the  $R = 0.24$  model we have

$$\frac{\sum_{\ell=2}^{10} (S/N)_{\ell}^2}{\sum_{\ell=2}^{100} (S/N)_{\ell}^2} \simeq 0.15.$$

One can say that that the  $TE$  correlation function directly probes the relic gravitational waves at recombination.

It emerges from this comparative analysis and Fig. 19 that both,  $TE$  and  $BB$ , methods need to be used, with the former one being more likely to bring the first identification of relic gravitational waves in the Planck data.

## X. CONCLUSIONS

A correct theoretical picture of the physical phenomenon is important for a proper setting of search experiment, as well as for the analysis of data and its interpretation. The relic gravitational waves ‘must be out there’, and we take this understanding as our starting point. Having further developed statistical theory of CMB anisotropies,

we concentrated on the  $TE$  correlation function. We have shown that the WMAP5  $TE$  data contain a hint on the presence of gravitational waves in the data. Our best-fit model includes a substantial amount of relic gravitational waves,  $R = 0.24$ . In simple terms, this means that 20% of the temperature quadrupole is caused by gravitational waves, and 80% by density perturbations. Because of large WMAP5 noises, the confidence of this conclusion is not high. The maximum likelihood result includes the WMAP's best-fit model with no gravitational waves,  $R = 0$ , almost within  $1\sigma$  interval.

We projected our conclusion  $R = 0.24$  on the forthcoming Planck mission. We numerically simulated Planck data and compared the  $TE$  and  $BB$  channels of observations. In the  $BB$  channel, much will depend on contamination by systematic effects. We distinguish the 'optimistic'  $BB$  case, when only the advertised instrumental noises are taken into account, and the 'realistic'  $BB$  case, when the effective noises are increased as a reflection of many possible residual effects. It is shown that the  $TE$  method will see the relic gravitational waves at a better than  $3\sigma$  level, whereas the 'realistic'  $BB$  method will see them at a better than  $2\sigma$  level.

Although most of our discussion focused on the Planck experiment, some balloon-borne [68, 69] and ground-based experiments [70, 71, 72, 73], currently in preparation, will be sensitive to part of the lower- $\ell$  spectrum of CMB. The contributions of various intervals of  $\ell$  to the total signal to noise ratio  $S/N$  can be read off from the evaluations developed here. These experiments will be complementary to the Planck mission and can provide a healthy competition in the race for discovery of relic gravitational waves.

## Acknowledgements

We appreciate useful mathematical discussions with N. N. Leonenko. WZ is partially supported by Chinese NSF grants No.10703005 and No.10775119.

## APPENDIX A: PROBABILITY DENSITY FUNCTION FOR $v_{\ell m}^{(c)}$

In Sec III B 3 it was shown that the joint pdf's  $f(\frac{a_{\ell 0}^{T(r)}}{\sqrt{2}}, \frac{a_{\ell 0}^{E(r)}}{\sqrt{2}})$ ,  $f(a_{\ell m}^{T(c)}, a_{\ell m}^{E(c)})$  (where  $m \geq 1$ ) are bivariate zero-mean normal distributions with standard deviations  $\frac{\sigma_{\ell}^T}{\sqrt{2}}$ ,  $\frac{\sigma_{\ell}^E}{\sqrt{2}}$  and correlation coefficient  $\rho_{\ell}$ . The indices  $\ell, m, c$  are considered fixed, so the two variables are distinguished by the labels  $T, E$ . From such a bivariate distribution one can derive a pdf for the product variable  $v_{\ell m}^{(c)} = a_{\ell m}^{T(c)} a_{\ell m}^{E(c)}$  (see Eq. 26). For each  $v_{\ell m}^{(c)}$ , the corresponding pdf is given by [74]

$$f(v_{\ell m}^{(c)}) = \frac{1}{\pi \sigma_{\ell}^T \sigma_{\ell}^E \sqrt{1 - \rho_{\ell}^2}} \exp \left[ \frac{v_{\ell m}^{(c)} \rho_{\ell}}{(1 - \rho_{\ell}^2) \sigma_{\ell}^T \sigma_{\ell}^E} \right] K_0 \left( \frac{|v_{\ell m}^{(c)}|}{(1 - \rho_{\ell}^2) \sigma_{\ell}^T \sigma_{\ell}^E} \right), \quad (\text{A1})$$

where  $K_0$  is the zero-order modified Bessel function.

Let us analyze the pdf (A1) in more detail. Firstly, Eq. (A1) shows that the pdf's with positive and negative  $\rho_{\ell}$  are related by

$$f(v_{\ell m}^{(c)}) \Big|_{-\rho_{\ell}} = f(-v_{\ell m}^{(c)}) \Big|_{\rho_{\ell}}. \quad (\text{A2})$$

If  $\rho_{\ell} = 0$  (no correlations), the pdf is symmetric with respect to the axis  $v_{\ell m}^{(c)} = 0$ . For any  $\rho_{\ell}$ , the pdf is divergent at  $v_{\ell m}^{(c)} = 0$ , because the modified Bessel function  $K_0(\alpha)$  is divergent at  $\alpha = 0$ .

In Fig. 21 we show the pdf's for different values of positive  $\rho_{\ell}$ . When  $\rho_{\ell}$  increases, the distribution shifts to the right reflecting the fact that the mean value  $\langle v_{\ell m}^{(c)} \rangle$  is proportional to  $\rho_{\ell}$ . In the limiting case  $\rho_{\ell} = 1$  the pdf develops a step, making  $f(v_{\ell m}^{(c)}) = 0$  for  $v_{\ell m}^{(c)} < 0$ . In general, using (6.621.3) from Ref. [35], one can show that the probabilities of negative, or positive, values of  $v_{\ell m}^{(c)}$  are given by

$$P(v_{\ell m}^{(c)} < 0) \equiv \int_{-\infty}^0 f(v_{\ell m}^{(c)}) dv_{\ell m}^{(c)} = \frac{2}{\pi} \frac{1 - \rho_{\ell}}{(1 - \rho_{\ell}^2)^{1/2}} F \left[ 1, \frac{1}{2}, \frac{3}{2}, \frac{\rho_{\ell} - 1}{\rho_{\ell} + 1} \right], \quad (\text{A3})$$

or

$$P(v_{\ell m}^{(c)} > 0) \equiv \int_0^{\infty} f(v_{\ell m}^{(c)}) dv_{\ell m}^{(c)} = \frac{2}{\pi} \frac{1 + \rho_{\ell}}{(1 - \rho_{\ell}^2)^{1/2}} F \left[ 1, \frac{1}{2}, \frac{3}{2}, \frac{\rho_{\ell} + 1}{\rho_{\ell} - 1} \right], \quad (\text{A4})$$

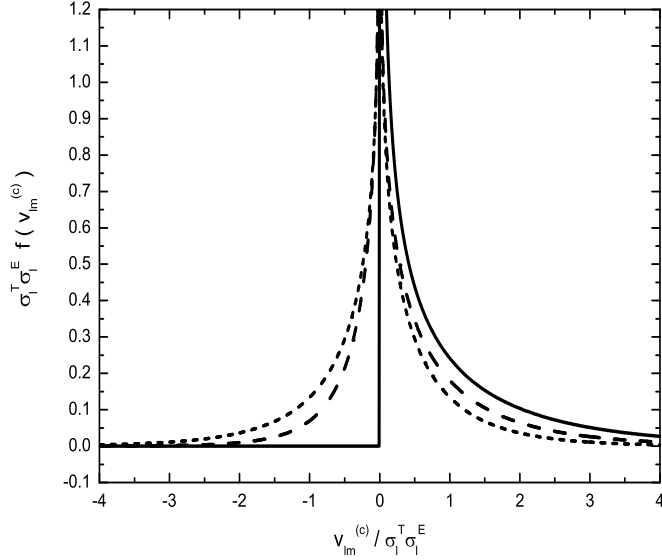


FIG. 21: Probability density functions  $f(v_{\ell m}^{(c)})$  for various positive  $\rho_{\ell}$ 's. The solid, dashed and dotted lines depict  $\rho_{\ell} = 1.0, 0.4,$  and  $0.0$ .

where  $F$  is the *hypergeometric*-function. These probabilities depend only on  $\rho_{\ell}$ , but not on  $\sigma_{\ell}^T$  and  $\sigma_{\ell}^E$ .

Similarly to what has been done in [74], one can show, using (9.131.1), (9.121.7), (1.624.9), (1.623.2) from [35], that  $P(v_{\ell m}^{(c)} < 0) + P(v_{\ell m}^{(c)} > 0) = 1$ , which confirms the correct normalization of  $f(v_{\ell m}^{(c)})$ . As expected, when  $\rho_{\ell} = 1$ ,  $P(v_{\ell m}^{(c)} < 0) = 0$  and  $P(v_{\ell m}^{(c)} > 0) = 1$ . And when  $\rho_{\ell} = 0$ ,  $P(v_{\ell m}^{(c)} < 0) = P(v_{\ell m}^{(c)} > 0) = 0.5$ .

The probability density function (A1) allows one to define the confidence intervals of finding specific values of  $v_{\ell m}^{(c)}$ . As an example, we start from the 68.3% confidence interval. We denote by  $(v_{\ell m}^{(c)})_U$  and  $(v_{\ell m}^{(c)})_L$  the upper and lower boundaries of the shortest interval, i.e. the interval having the minimum difference  $(v_{\ell m}^{(c)})_U - (v_{\ell m}^{(c)})_L$ , such that [75]

$$\int_{(v_{\ell m}^{(c)})_L}^{(v_{\ell m}^{(c)})_U} f(v_{\ell m}^{(c)}) d v_{\ell m}^{(c)} = 0.683.$$

The surface area under the pdf curve between  $(v_{\ell m}^{(c)})_U$  and  $(v_{\ell m}^{(c)})_L$  gives the probability (68.3%) of finding  $v_{\ell m}^{(c)}$  in this interval. This is a sensible measure [75] of uncertainty of our estimator. For the pdf's that we are dealing with, the 68.3% confidence interval always includes points of the maximum and the mean value of the pdf.

In Fig. 22, we plot the 68.3%, 95.4%, 99.7% confidence intervals for different  $\rho_{\ell}$ 's. When  $\rho_{\ell} = 0$ , the confidence intervals are symmetric with respect to the mean value (zero) of  $v_{\ell m}^{(c)}$ . When  $\rho_{\ell}$  increases, the intervals move toward larger values  $v_{\ell m}^{(c)}$ . In the limit  $\rho_{\ell} \rightarrow 1$ , the lower boundary  $(v_{\ell m}^{(c)})_L$  approaches 0 for all levels of confidence. For any confidence level, the confidence interval is not symmetric with respect to the mean value of  $v_{\ell m}^{(c)}$ . It can also be seen that, unless  $\rho_{\ell} \approx 1$ , there is a significant probability of finding  $v_{\ell m}^{(c)} < 0$ , despite the fact that the mean value is strictly non-negative.

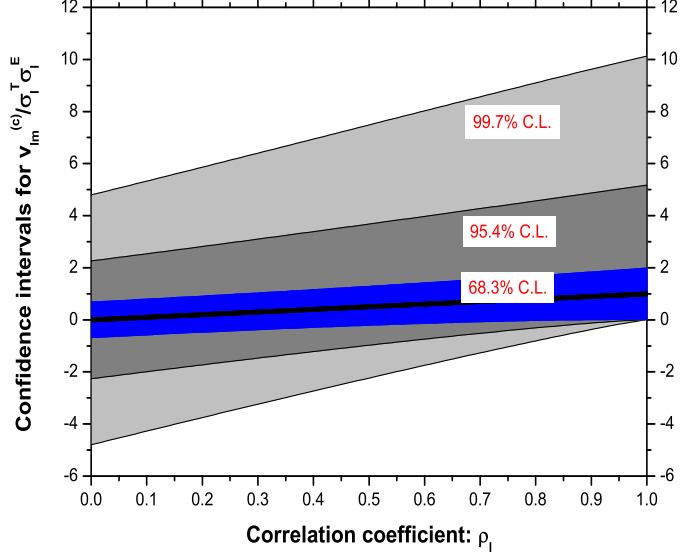


FIG. 22: The 68.3%, 95.4% and 99.7% confidence intervals of the variable  $v_{lm}^{(c)}/\sigma_l^T \sigma_l^E$  for different  $\rho_\ell$ . The solid (black) line denotes the mean value of  $v_{lm}^{(c)}/\sigma_l^T \sigma_l^E$ .

## APPENDIX B: SOME PROPERTIES OF $f(D_\ell^{TE})$

It is insightful to discuss properties of  $f(D_\ell^{TE})$  in comparison with  $f(v_{lm}^{(c)})$  in Eq. (A1). Surely, both functions go to zero when the argument  $\rightarrow \pm\infty$ . But the behaviors at zero argument are different,  $f(D_\ell^{TE})$  does not diverge at  $D_\ell^{TE} = 0$  if  $n > 1$ . Although the modified Bessel functions do diverge at zero argument [35],

$$K_\nu(\alpha) \sim \frac{(\nu - 1)!}{2} \left(\frac{\alpha}{2}\right)^{-\nu}, \quad \text{where } (\nu \geq 1, \alpha \rightarrow 0),$$

the first factor in the right hand side of Eq. (31) compensates for this divergency, so that the pdf (31) remains finite.

In the limit  $\rho_\ell \rightarrow 1$ , keeping other parameters fixed and using the asymptotic formula [35]  $K_\nu(\alpha) \sim \sqrt{\frac{\pi}{2\alpha}} e^{-\alpha}$  for  $\alpha \rightarrow \infty$ , one obtains

$$f(D_\ell^{TE}) \rightarrow \frac{n\tilde{V}^{n/2-1} e^{-\tilde{V}/2}}{2^{n/2}\Gamma(n/2)\sigma_\ell^T \sigma_\ell^E} \quad \text{with } \tilde{V} \equiv \frac{nD_\ell^{TE}}{\sigma_\ell^T \sigma_\ell^E}.$$

As expected, the asymptotic distribution is a  $\chi^2$  distribution with  $n$  degrees of freedom.

Similarly to Eq. (A2) one has

$$f(D_\ell^{TE}) \Big|_{-\rho_\ell} = f(-D_\ell^{TE}) \Big|_{\rho_\ell}$$

The probability of negative, or positive, values of  $D_\ell^{TE}$  is given by

$$\begin{aligned} P(D_\ell^{TE} < 0) &\equiv \int_{-\infty}^0 f(D_\ell^{TE}) dD_\ell^{TE} = \frac{(1 - \rho_\ell)(1 - \rho_\ell^2)^{\frac{n}{2}-1}}{2^{n-1}} \\ &\times \frac{\Gamma(n)}{\Gamma(\frac{n}{2} + 1)\Gamma(\frac{n}{2})} F\left[1, 1 - \frac{n}{2}, 1 + \frac{n}{2}, \frac{\rho_\ell - 1}{\rho_\ell + 1}\right], \end{aligned} \quad (\text{B1})$$

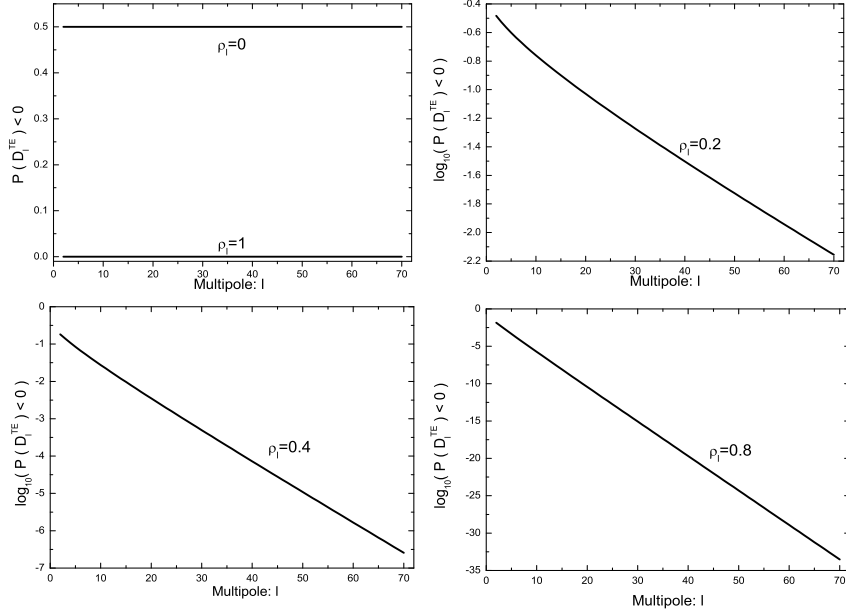


FIG. 23:  $P(D_\ell^{TE} < 0)$  as a function of  $\ell$  for  $\rho_\ell = 0.0, 0.2, 0.4, 0.8, 1.0$ . In the upper left panel the vertical axis is  $P(D_\ell^{TE} < 0)$ , whereas in other three panels it is  $\log_{10} P(D_\ell^{TE} < 0)$ .

or

$$\begin{aligned}
P(D_\ell^{TE} > 0) &\equiv \int_0^{+\infty} f(D_\ell^{TE}) dD_\ell^{TE} = \frac{(1 + \rho_\ell)(1 - \rho_\ell^2)^{\frac{n}{2}-1}}{2^{n-1}} \\
&\times \frac{\Gamma(n)}{\Gamma(\frac{n}{2} + 1)\Gamma(\frac{n}{2})} F\left[1, 1 - \frac{n}{2}, 1 + \frac{n}{2}, \frac{\rho_\ell + 1}{\rho_\ell - 1}\right]. \tag{B2}
\end{aligned}$$

These probabilities depend on  $\rho_\ell$  but not on  $\sigma_\ell^T, \sigma_\ell^E$ . As it should be, Eqs. (B1, B2) reduce to Eqs. (A3, A4) when  $n = 1$ .

We have checked numerically, for a set of  $\ell$ 's and  $\rho_\ell$ 's, the normalization condition  $P(D_\ell^{TE} < 0) + P(D_\ell^{TE} > 0) = 1$ . A useful equality relating the probabilities for positive and negative  $\rho_\ell$ 's is

$$P(D_\ell^{TE} < 0) \Big|_{-\rho_\ell} = 1 - P(D_\ell^{TE} < 0) \Big|_{\rho_\ell} .$$

A similar equality is valid for probabilities  $P(D_\ell^{TE} > 0) \Big|_{\pm\rho_\ell}$ . When  $\rho_\ell = 1$ , we find, using formula  $F[1, 1 - \frac{n}{2}, 1 + \frac{n}{2}, 0] = 1$ , that  $P(D_\ell^{TE} < 0) = 0$  for any  $n$ . On the other hand, when  $\rho_\ell = 0$ , we find, using formula  $F[1, 1 - \frac{n}{2}, 1 + \frac{n}{2}, -1] = \frac{\sqrt{\pi} \Gamma(\frac{n}{2} + 1)}{\Gamma(\frac{n}{2})}$ , that  $P(D_\ell^{TE} < 0) = P(D_\ell^{TE} > 0) = \frac{1}{2}$  for any  $n$ .

In Fig. 23, we plot the probability  $P(D_\ell^{TE} < 0)$  in the interval  $2 \leq \ell \leq 70$  for selected values of  $\rho_\ell$ ,  $\rho_\ell = 0.0, 0.2, 0.4, 0.8$  and  $1.0$ . It is seen that for a fixed  $\rho_\ell$  the value of  $P(D_\ell^{TE} < 0)$  rapidly decreases as  $\ell$  becomes larger, excepting the limiting cases  $\rho_\ell = 0$  or  $1$ . For a fixed  $\ell$  and growing  $\rho_\ell$ , the  $P(D_\ell^{TE} < 0)$  changes from  $0.5$  to  $1$ .

- 
- [1] L. P. Grishchuk, Zh. Eksp. Teor. Fiz. **66**, 833 (1974) [ Sov. Phys. JETP **39**, 402 (1974)].
- [2] L. P. Grishchuk, *Discovering Relic Gravitational Waves in Cosmic Microwave Background Radiation*, Chapter in the “Wheeler book”, edited by I. Ciufolini and R. Matzner, (Springer, 2008) (in press); arXiv:0707.3319.
- [3] D. Baskaran, L. P. Grishchuk and A. G. Polnarev, Phys. Rev. D **74** 083008 (2006).
- [4] E. Komatsu *et al.*, arXiv:0803.0547.
- [5] N. L. Johnson and S. Kotz, *Distributions in Statistics: Continuous Multivariate Distributions* (John Wiley and Sons, Inc. New York, 1972).
- [6] B. V. Gnedenko, *The Theory of Probability* (Chelsea Publishing Company, New York, 1962).
- [7] C. -P. Ma and E. Bertschinger, Astrophys. J. **455**, 7 (1995).
- [8] M. Zaldarriaga and U. Seljak, Phys. Rev. D **55**, 1830 (1997).
- [9] L. D. Landau and E. M. Lifshitz, *The Classical Theory of Fields*, 4th rev. engl. ed. (Pergamon Press, Oxford, 1975).
- [10] M. Kamionkowski, A. Kosowsky and A. Stebbins, Phys. Rev. D **55**, 7368 (1997).
- [11] A. G. Polnarev, Sov. Astron. **29**, 607 (1985).
- [12] M. White, Phys. Rev. D **46**, 4198 (1992).
- [13] L. M. Krauss and M. White, Phys. Rev. Lett. **69**, 869 (1992).
- [14] R. Crittenden, J. R. Bond, R. L. Davis, G. Efstathiou and P. J. Steinhardt, Phys. Rev. Lett. **71**, 324 (1993).
- [15] L. P. Grishchuk, Phys. Rev. D **48**, 3513 (1993); Phys. Rev. Lett. **70**, 2371 (1993).
- [16] R. A. Frewin, A. G. Polnarev and P. Coles, Mon. Not. R. Astron. Soc. **266**, L21 (1994).
- [17] W. Hu and N. Sugiyama, Astrophys. J. **444**, 489 (1995).
- [18] M. Zaldarriaga and D. D. Harari, Phys. Rev. D **52**, 3276 (1995).
- [19] S. Bose and L. P. Grishchuk, Phys. Rev. D **66**, 043529 (2002).
- [20] J. R. Pritchard and M. Kamionkowski, Ann. Phys. (N.Y.) **318**, 2 (2005).
- [21] B. G. Keating *et al.*, Int. J. Mod. Phys. A **21**, 2459 (2006).
- [22] W. Zhao and Y. Zhang, Phys. Rev. D **74**, 083006 (2006).
- [23] R. Flauger and S. Weinberg, Phys. Rev. D **75**, 123505 (2007).
- [24] D. M. Brink and G. R. Satchler, *Angular Momentum* (Clarendon Press, Oxford, 1968).
- [25] U. Seljak and M. Zaldarriaga, Phys. Rev. Lett. **78**, 2054 (1997).
- [26] M. Kamionkowski, A. Kosowsky and A. Stebbins, Phys. Rev. Lett. **78**, 2058 (1997).
- [27] A. Lue, L. Wang, and M. Kamionkowski, Phys. Rev. Lett. **83**, 1506 (1999).
- [28] T. Kahniashvili, G. Gogoberidze and B. Ratra, Phys. Rev. Lett. **100**, 231301 (2008).
- [29] L. Knox, Phys. Rev. D **52**, 4307 (1995).
- [30] L. P. Grishchuk and J. Martin, Phys. Rev. D **56**, 1924 (1997).
- [31] D. J. Mortlock, A. D. Challinor and M. P. Hobson, Mon. Not. R. Astron. Soc. **330**, 405 (2002).
- [32] A. Lewis, A. Challinor and N. Turok, Phys. Rev. D **65**, 023505 (2001).
- [33] L. Perotto *et al.*, J. Cosmol. Astropart. Phys. **0610**, 013 (2006).
- [34] A. G. Polnarev, N. J. Miller and B. G. Keating, Mon. Not. R. Astron. Soc. **386**, 1053 (2008); N. J. Miller, A. G. Polnarev and B. G. Keating, arXiv:0710.3651 (2007).
- [35] I. S. Gradshteyn and I. M. Ryzhik, *Table of integrals, Series and Products* (Academic Press, New York, 1965).
- [36] J. Dunkley *et al.*, arXiv:0803.0586.
- [37] M. S. Turner and M. White, Phys. Rev. D **53**, 6822 (1996).
- [38] U. Seljak and M. Zaldarriaga, Astrophys. J. **469**, 437 (1996).
- [39] A. Lewis, A. Challinor and A. Lasenby, Astrophys. J. **538**, 473 (2000).
- [40] L. P. Grishchuk, Phys. Rev. D **50**, 7154 (1994).
- [41] Legacy Archive for Microwave Background Data, <http://lambda.gsfc.nasa.gov/product/map/current/>.
- [42] L. Page *et al.*, Astrophys. J. Suppl. **170**, 335 (2007).
- [43] L. Page *et al.*, Astrophys. J. Suppl. Ser. **148**, 39 (2003).
- [44] Planck Collaboration, arXiv:astro-ph/0604069.
- [45] A. Kogut *et al.*, Astrophys. J. Suppl. Ser. **148**, 161 (2003).
- [46] G. Hinshaw *et al.*, arXiv:0803.0732.
- [47] M. R.olta *et al.*, arXiv:0803.0593.
- [48] A. Lewis, Phys. Rev. D **78**, 023002 (2008).
- [49] S. Hamimeche and A. Lewis, Phys. Rev. D **77**, 103013 (2008).
- [50] L. Verde *et al.*, Astrophys. J. Suppl. Ser. **148**, 195 (2003).
- [51] E. Komatsu *et al.*, Astrophys. J. Suppl. Ser. **148**, 119 (2003).
- [52] B. Gold *et al.*, arXiv:0803.0715.
- [53] L. A. Page, in *Critical Dialogues in Cosmology*, edited by N. Turok (Singapore: World Science, 1997).
- [54] J. R. Bond, A. H. Jaffe and L. E. Knox, Astrophys. J. **533**, 19 (2000).
- [55] S. Podariu *et al.*, Astrophys. J. **559**, 9 (2001).
- [56] J. R. Green and D. Margerison, *Statistical treatment of experimental data* (Elsevier Scientific Publishing Company, New York, 1977).
- [57] A. Lewis and S. Bridle, Phys. Rev. D **66**, 103511 (2002).

- [58] D. N. Spergel *et al.*, *Astrophys. J. Suppl. Ser.* **170**, 377 (2007).
- [59] A. Amblard, A. Cooray and M. Kaplinghat, *Phys. Rev. D* **75**, 083508 (2007).
- [60] M. Shimon, B. Keating, N. Ponthieu and E. Hivon, *Phys. Rev. D* **77**, 083003 (2008).
- [61] A. Lewis and A. Challinor, *Phys. Rep.* **429**,1 (2006).
- [62] R. G. Crittenden, D. Coulson and N. G. Turok, *Phys. Rev. D* **52**, R5402 (1995).
- [63] A. Melchiorri and C. J. Odman, *Phys. Rev. D* **67**, 021501(R) (2003).
- [64] A. Stuart, J. K. Ord and S. Arnold, *Kendall's Advanced theory of Statistics, Volume 2A* (Arnold publishers, London, 1999).
- [65] M. Tegmark, A. Taylor and A. Heavens, *Astrophys. J.* **480**, (1997) 22.
- [66] A. H. Jaffe, M. Kamionkowski and L. Wang, *Phys. Rev. D* **61**, 083501 (2000).
- [67] X. Fan, C. L. Carilli and B. Keating, *Ann. Rev. Astron. Astrophys.* **44**, 415 (2006).
- [68] P. Oxley *et al.*, astro-ph/0501111.
- [69] B. P. Crill *et al.*, arXiv:0807.1548.
- [70] B. G. Keating *et al.*, in *Polarimetry in Astronomy*, edited by Silvano Fineschi, *Proceedings of the SPIE*, **4843** (2003).
- [71] C. Pryke *et al.*, QUaD collaboration, arXiv:0805.1944.
- [72] A. C. Taylor, Clover Collaboration, *New Astron. Rev.* **50**, 993 (2006).
- [73] D. Samtleben, arXiv:0806.4334.
- [74] L. P. Grishchuk, *Phys. Rev. D* **53**, 6784 (1996).
- [75] D. S. Sivia, *Data Analysis, A Bayesian Tutorial* (Oxford University Press, Oxford, 1996).